

# Modelling subglacial water using Navier-Stokes flow

Masterarbeit im Studiengang Marine Geosciences

Fachbereich Geowissenschaften  
Universität Bremen

von

Hans Leonard Rossmann

March 14, 2015

First supervisor: Prof. Dr. Angelika Humbert

Second supervisor: Dr. Torsten Bickert





---

Name

**Declaration acc. to § 10 Paragraph 11 Common Part of the Master Examination Regulations**

I hereby declare that I wrote my Master Thesis independently and that I did not use other sources and auxiliary means than the ones indicated.

This Master Thesis is not submitted in another examining procedure.

Place/Date: \_\_\_\_\_

Signature: \_\_\_\_\_



## Abstract

This Master thesis investigates the formation and evolution of subglacial drainage systems underneath ice sheets. The presence of water underneath ice masses has enormous effects on ice dynamics as it acts as a lubricant. Ice sheets play a big role in ocean circulation and climate dynamics. So far little is known about the formation and evolution of subglacial water. However, various elements of hydrological systems are suggested to exist ranging from thin water sheets to channels and lakes. This Master thesis attempts to fill this gap and creates a conceptual thermo-mechanical model of ice and water dynamics, which is solved using the finite element method.

While the Stokes-equation is used for ice, the Navier-Stokes equation is introduced for the simulation of the water flow. Thus the acceleration terms are included. A coupling of water and ice flow has to overcome the problem that water flows on short time scales while ice on long once. This problem is solved with an adaptive timestepping mode. In order to evolve a water layer the melt rates are calculated by a state of the art enthalpy formulation, using the advantage of solving for temperature and water content at the once.

The results demonstrate that it is possible to model both ice and water flow within one approach using the Navier-Stokes flow and the enthalpy formulation. The experiments investigate the effects of geothermal heat flux and inflow velocities on the melt rate behaviour. The results show that thin water layers develop into a channelized flow form when a certain threshold in the water velocity is overcome. Moreover, cavities form in regions of increased geothermal heat flux. With increasing inflow velocity the cavity propagates further in the direction of flow. The results demonstrate a strong relationship between water flow velocities and changes in melt dynamics. Further, it illustrates that the subglacial water system is under constant change. Hence, this study gives an important insight into melt dynamics under ice masses and their evolution.



# Contents

<b>Contents</b>	<b>v</b>
<b>1. Introduction</b>	<b>1</b>
1.1. Subglacial water . . . . .	3
1.2. Aims and Objectives . . . . .	5
<b>2. Theory</b>	<b>7</b>
2.1. Balance Equations . . . . .	7
2.1.1. Mass balance . . . . .	7
2.1.2. Momentum balance . . . . .	7
2.1.3. Enthalpy formulation . . . . .	8
2.1.4. Enthalpy balance . . . . .	9
2.2. Constitutive equations and rheology of ice . . . . .	10
2.2.1. Incompressible Newtonian flow . . . . .	10
2.2.2. Incompressible Non-Newtonian fluids and the rheology of ice . . . . .	10
2.2.3. Glen's flow law . . . . .	11
2.3. Boundary conditions . . . . .	12
2.3.1. Ice surface . . . . .	13
2.3.2. Ice base . . . . .	13
2.3.3. Ice water interface . . . . .	14
2.3.4. Lateral boundaries . . . . .	15
<b>3. The numerical model</b>	<b>17</b>
3.1. Implementation . . . . .	17
3.1.1. Geometry . . . . .	17
3.1.2. Switch values . . . . .	19
3.1.3. Mesh . . . . .	20
3.1.4. Arbitrary Lagrangian Method (ALE), Moving Mesh . . . . .	20
3.1.5. Heat transfer in fluids . . . . .	21
3.1.6. Laminar flow 1 + 2 . . . . .	24
3.1.7. Solver . . . . .	28
<b>4. Experiments and Results</b>	<b>31</b>
4.1. Experiments . . . . .	31

4.2. Results . . . . .	33
4.2.1. Verification . . . . .	33
4.2.2. Exp: <i>sub_m1</i> . . . . .	38
4.2.3. Exp: <i>sub_m2</i> . . . . .	40
4.2.4. Exp: <i>sub_m2-flat</i> . . . . .	43
4.2.5. Exp: <i>sub_m3</i> . . . . .	44
<b>5. Discussion</b>	<b>47</b>
5.1. Verification experiments . . . . .	47
5.2. Feasibility of modelling subglacial water using Navier-Stokes flow . . . . .	48
5.3. Experiments <i>sub_m1-3</i> . . . . .	50
5.3.1. Experiment <i>sub_m1</i> . . . . .	50
5.3.2. Experiment <i>sub_m2</i> . . . . .	52
5.3.3. Experiment <i>sub_m3</i> . . . . .	55
5.4. Intercomparison <i>sub_m1-3</i> . . . . .	57
5.5. Implications . . . . .	57
<b>6. Conclusion and Outlook</b>	<b>63</b>
<b>Bibliography</b>	<b>67</b>
<b>List of Figures</b>	<b>71</b>
<b>List of Tables</b>	<b>73</b>
<b>A. Appendix</b>	<b>75</b>

# 1. Introduction

Glacier ice covers nearly 10% of the today's Earth surface (Cuffey and Paterson, 2010). These glaciated areas play a major role in the Earth system. Changes in the cryosphere have effects the Earth's energy budget via changes in albedo or changes in sea level due to accumulation or release of fresh water. The effect of fresh water into the ocean has two major effects. First, when fresh water enters into the regions of deep water formations (e.g. the North Atlantic) it changes the whole Meridional Overturning Circulations (MOC) due to density decreases of the water masses (Rahmstorf, 2006; Delworth, 2008). This triggers changes in climate conditions and heat transport via ocean circulations (Rahmstorf, 2006). Second the change in sea level due to mass loss or gain from the land ice sheets. The Greenland and the Antarctic ice sheets sum up to a potential sea level rise of 65.66 m (Solomon et al., 2007), when completely molten. The ice sheets will not melt completely in the near future but an increased volume change has been recorded in the last years. The volume loss of Greenland and Antarctica combined is  $-503 \pm 107 \text{ km}^3 \text{ yr}^{-1}$  between 2003 and 2009 (Helm et al., 2014). In Greenland the mass loss divides into  $\sim 50\%$  by melting and  $\sim 50\%$  by calving. Whereas, in Antarctica the major mass loss is due to calving (ca. 98%) and only 2% due to melting (Shepherd et al., 2012). Therefore, it is of interest to analyse the contribution of these mass losses.

On an ice sheet mass is accumulated via precipitation in form of snow. It can lose mass due to sublimation, melting including run off and calving and transport over the grounding line into an ice shelf. Since the last two are the dominant process in Antarctica, it is an aim of this study to investigate effects, which contribute to the mass losses. In an ice sheet mass is transported via outlet glaciers or ice streams from the interior to the edges. Here, glaciers either terminated on land, on sea or in ice shelves. For the later one, the transport of ice over the grounding line is important. The grounding line is the region where ice stream or glaciers lose contact to the bedrock and the ice gets afloat. At that point the ice already contributes to sea level change due to the hydrostatic equilibration.

The transport of ice in these outlet glaciers and ice streams is a result of their ice dynamics. Ice can flow via creep flow, a deformation on a grain scale basis (Cuffey and Paterson, 2010), which has flow rates ranging from  $1 \text{ m yr}^{-1}$  to several hundred meters per year (Rignot et al., 2011) depending on the applied stress. Whereas, the high end velocities in ice streams, which can reach up to kilometres per year (see Fig. 1.2), are not only due to creep deformation of the ice itself but due to a combination of creep flow and sliding over the bedrock. The sliding occurs if the ice masses are not frozen to the ground (so called temperate base) and liquid water (subglacial water) is present at the base. Liquid water

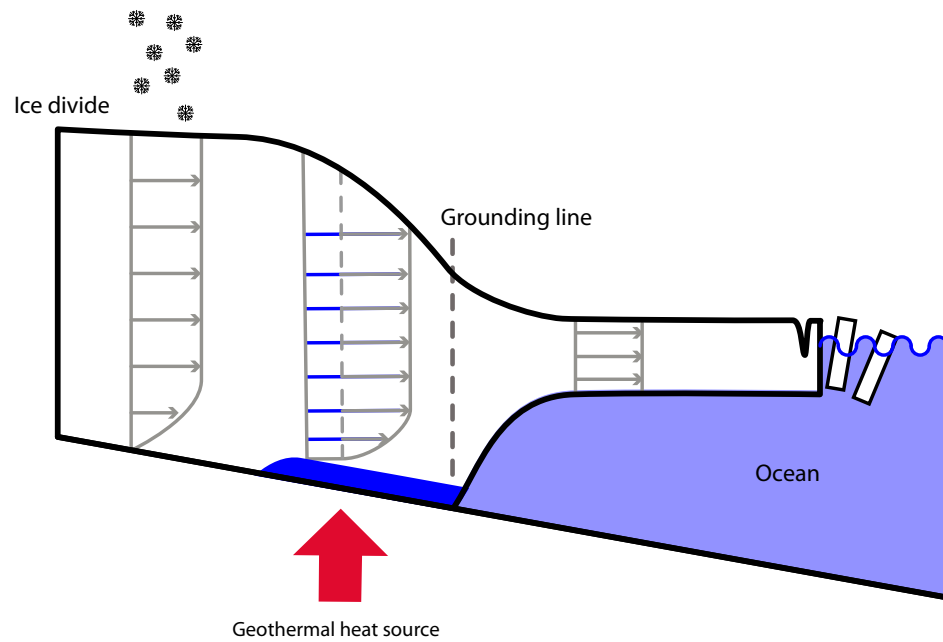


Figure 1.1.: Schematic drawing of mass transported in ice sheets and velocity fields.

has an enormous lubrication effect on the ice. Ice mass dynamics are strongly influenced by the conditions at the bedrock. The subglacial water has different forms of appearance underneath an ice mass, which is described in the next section. As the ice dynamics is influenced by the presence of water, so is the heat transfer and temperature regime of an ice mass. If subglacial water flows between the bedrock and the ice mass, it can transport heat faster than ice. This has effects on the melt dynamics at the base and therefore on the evolution of the subglacial drainage systems. Hence, it is benefit to study the effects of melt dynamics linked to water flow to give assumption about the formation and effect of subglacial water systems.

Up to now only few field surveys have been done, as it is difficult to localize the water bodies underneath ice masses. There have been dye trace measurements, analysis of glacier relict areas, bore hole measurements and camera surveys (Benn and Evans, 2010). These studies suffer a long-term evolution record of these systems, which is hardly achievable. Nevertheless, since the last decade the existence of subglacial water under ice sheet has been proven (Kleiner and Humbert, 2014; Benn and Evans, 2010; Cuffey and Paterson, 2010; Siegert, 2000) and its important effects on ice dynamics and melt dynamics is not negligible (Fricker et al., 2007). In order to examine the changes in subglacial hydrological systems over a longer period numerical models are necessary and can achieve this goal. They can predict changes in these subglacial systems, according to the implemented equations. The aim of this study is now to create a numerical model, which links ice flow, water flow and heat transfer in one. This enables to study the evolution of subglacial systems. The

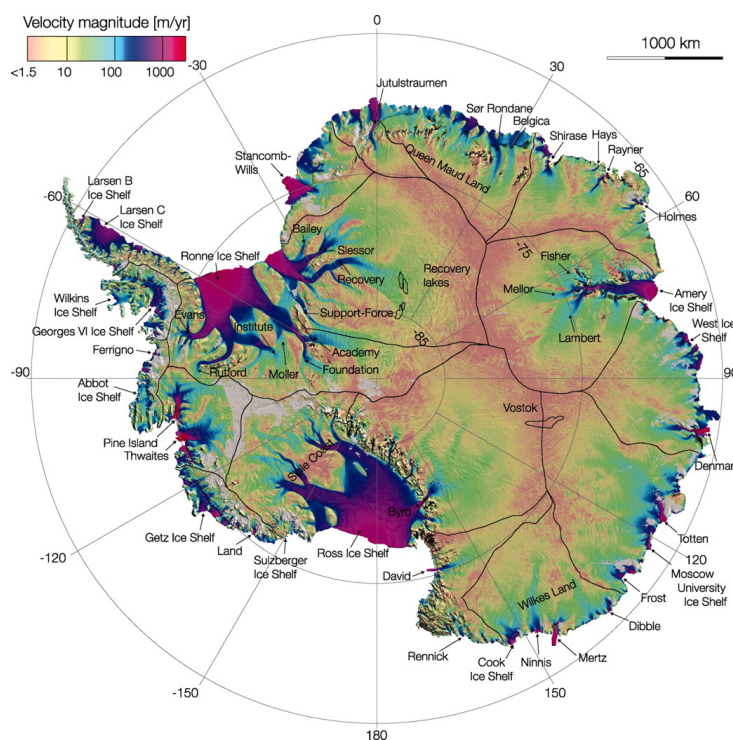


Figure 1.2.: Surface velocities of Antarctica with clearly visible high velocities in outlet glaciers and ice streams (Rignot et al., 2011)

Navier-Stokes equation is common in Computational Fluid Dynamics (CFD). It can predict the flow in laminar and turbulent regimes. Further, it will enable to model the high viscous flow of ice and the low viscous flow of water. Using the same equation to model different flow brings the advantage that these flow can be modelled at the same time. Up to now in numerical models only parameterizations of the subglacial water flow are implemented like in Kleiner and Humbert (2014). This master thesis therefore fills the gap of modelling the evolution of subglacial systems with the help of a numerical model. The following quote by Benn and Evans underlines the need of further investigation in glaciers hydrology: "In the last decade or so, considerable advances have been made in our understanding of glacial hydrological systems, and our ability to represent them in glacier models has improved immensely. However, the statement made by Arnold et al. (1998), that much work remains to be done in terms of field observations, modelling and development of theory of glacier hydrological systems, is no less true today than when it was written." (Benn and Evans, 2010).

## 1.1. Subglacial water

Subglacial water describes all possible water flows beneath ice masses or glaciers. The water origins either from above the glacier, created by melting processes or from geothermal heating or frictional heating by the ice movement itself or strain heating. This raises the temperature to the pressure melting point. All surplus energy is then used for melting of

the ice. Once the water is present it can either gather in hydro potential sinks and form lakes underneath the ice sheet or it can be transported. There are five basic drainage systems, which can transport water. Bulk movement of water with deforming tilt, Darcian pore water flow, Dendritic channel network, Braided canal network, Linked cavity and Thin water film (see Fig.1.3(b) to 1.3(d)) (Benn and Evans, 2010; Glasser, 2013; Fountain and Walder, 1998).

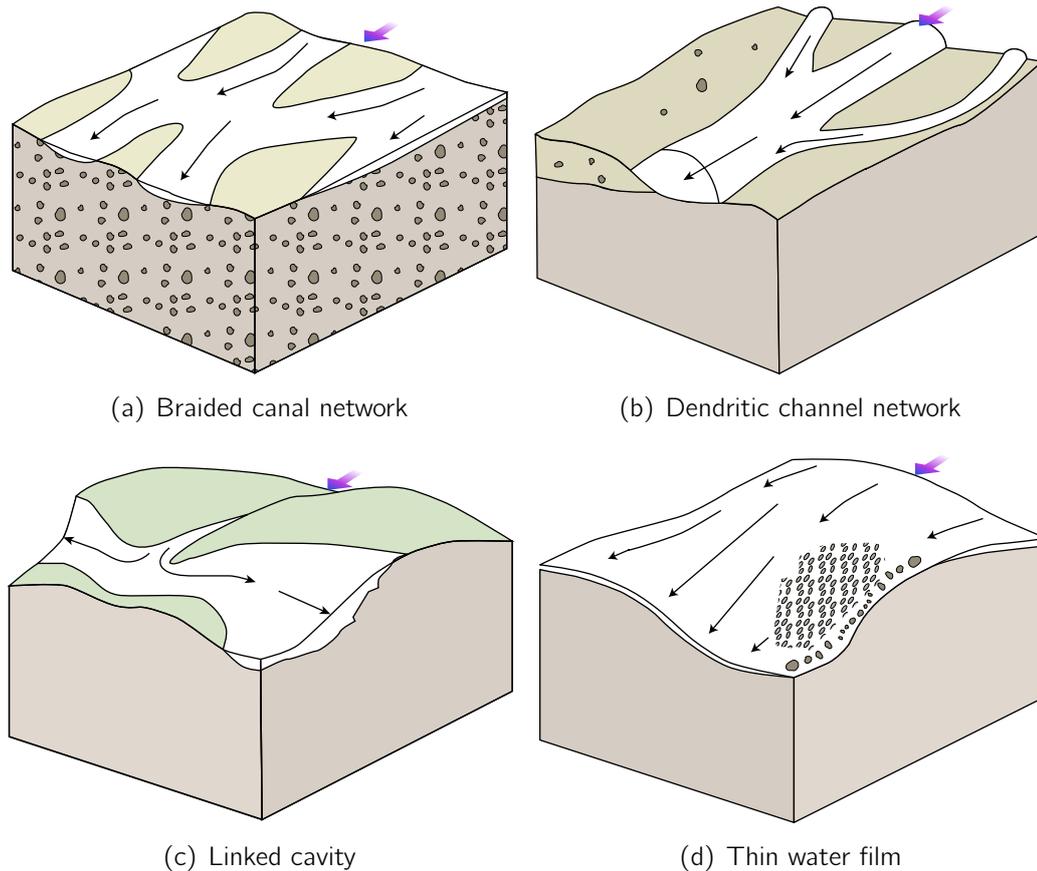


Figure 1.3.: Schematic drawings of subglacial drainage systems (modified after Benn and Evans (2010))

From Alpine glacier it is known that changes in these drainage systems control the ice dynamics. This linkage is well studied for surging glaciers. This type of glacier has a periodical fast and slow flow phase. One of the intensively studied glacier is the Variegated Glacier, in southern Alaska, (Murray, 2003). The surge behaviour of this glacier is linked to the change from a linked cavity system during the fast flow to a channelised drainage system which terminates the fast flow period (Murray, 2003; Kamb, 1987). These drainage systems are present underneath ice sheets as well. So the following thought experiments are potential effects of the named drainage systems. The effect of a thin film of water could lead to an increased ice velocities, since the enhance lubrication effect Fountain and

Walder (1998). Linked cavities could have the same effect as the thin film as they appear over a broad region. They are supposed to be more stable than the thin film. In these both systems the water flow is slow. They are regarded as inefficient drainage systems. Therefore, the heat in these both systems is mainly transported via a diffusion process. In contrast to them the channelized systems are fast flowing systems, where water is drained rapidly. Therefore, heat is transported mainly via advection. Further, turbulent flow regimes are able to establish, which influences the heat transport, too. Their localized appearance should have a lower effect than the linked cavities or the thin film has on the ice dynamics. Overall the subglacial drainage systems can shape the thermal and the dynamic regime of glaciers and ice masses.

## 1.2. Aims and Objectives

The aim of this master thesis is to generate a numerical model, which describes the ice and water flow at the same time. Further a heat transfer module shall be implemented in order to model melt and refreezing process in subglacial systems.

The coupling of heat transfer and flow modelling with the Navier-Stokes equation has not yet been implemented in ice models. There is the difficulty of coupling the fast flow of water with the slow of ice. Therefore, one part of the thesis investigates the possible linkage between these two flow types. Further the state of the art Enthalpy formulation from (Aschwanden et al., 2012) is used to model the thermodynamics. The aim of this thesis is to create a conceptual two-dimensional numerical model, which reflects the conditions of an ice sheet and incorporates the named physical principles. Additionally different experiments shall give an insight into melt dynamics underneath ice masses.

The key scientific research questions are here: How can subglacial channels form underneath ice masses? What are the effects of flowing water on the heat transfer in subglacial systems? How do cavities form and evolve underneath the ice. Since these in numerical model and field observations these question have not be answered, this Master thesis attempts to show that the flow velocities in subglacial drainage systems have enormous impact on their evolution and creation. The presents of water at the base and its velocities are in constantly changing system.



## 2. Theory

In this Chapter the theoretical foundation is given for the numerical model. On long time scales glacier ice behaves like a fluid. Therefore, it can be described using continuum mechanics. With the help of fluid dynamics, which is a branch of continuum mechanics, the governing equations describe the flow and thermal state of ice and water. The governing equations are the mass balance equation (section 2.1.1), momentum balance equation (section 2.1.2) and the energy balance equation (section 2.1.4). Constitutive equations (Section 2.2) are needed to complete the system. Here only the most important equations are presented as a full derivation of the equation would exceed the scope of this thesis. Furthermore, they are described in detail by (eg. Greve and Blatter (2009)). The theory of the enthalpy formulations (heat transfer) was first described by Aschwanden et al. (2012) and only the most important equations are displayed here. The numerical method of finite elements is applied to solve the partial differential equations.

### 2.1. Balance Equations

#### 2.1.1. Mass balance

Pure glacier ice and water are incompressible fluids. The mass balance of an incompressible continuum can be written as:

$$\operatorname{div}(\mathbf{v}) = 0, \quad (2.1)$$

which states that the velocity field  $\mathbf{v}$  is source and sink free.

#### 2.1.2. Momentum balance

The momentum balance engages from Newton's second law. The change of momentum over time has to be in equilibrium with all forces applied on the body. These forces can either be external volume forces  $\mathbf{f}$  acting on each element of the body such gravity or Coriolis force, or internal stresses  $\boldsymbol{\sigma}$  which act on the body's boundary surface. The momentum balance for momentum density ( $\rho\mathbf{v}$ ) reads:

$$\frac{\partial \rho\mathbf{v}}{\partial t} + \operatorname{div}(\rho\mathbf{v}\mathbf{v}) = \operatorname{div}(\boldsymbol{\sigma}) + \mathbf{f}. \quad (2.2)$$

The equation 2.2 is as well called the Navier-Stokes equation. It can be rewritten as followed in its incompressible form:

$$\rho \cdot (\partial_t \mathbf{v} + \mathbf{v} \nabla \mathbf{v}) = -\nabla p + \rho \mathbf{g} + \eta \nabla^2 \mathbf{v}. \quad (2.3)$$

The Navier-Stokes equation links the velocity term ( $\partial_t \mathbf{v}$ ) and the turbulent term ( $\mathbf{v} \nabla \mathbf{v}$ ) of a fluid parcel on the left hand side to the pressure derivatives ( $-\nabla p$ ), the gravity ( $\rho \mathbf{g}$ ) acting on the parcel and the fluids viscosity term ( $\eta \nabla^2 \mathbf{v}$ ) on the right hand side. The ratio between inertial forces ( $-\nabla p + \rho \mathbf{g}$ ) to viscous forces ( $\eta \nabla^2 \mathbf{v}$ ) is expressed by the dimensionless Reynold's number ( $Re$ ) for a given flow condition. When the  $Re$  number exceeds a critical value the flow type changes from laminar flow to turbulent flow.

**Water:** The  $Re$  number of water is high since the viscosity is low ( $\eta_{water} \approx 1.78 \cdot 10^{-3} Pa s$ ). Water can flow in a laminar or turbulent regime depending on the flow velocity. In order to calculate the flow of water the whole Navier-Stokes equation has to be solved, thus

**Ice:** On the other side, ice has a high viscosity, 17 magnitudes larger than water, and therefore a low Reynold's number ( $Re \approx 10^{-10}$ ) (Lliboutry, 1987). Thus the inertial forces, on the left hand side of the equ. 2.2, can be neglected. Equation 2.2 than simplify to:

$$div(\boldsymbol{\sigma}) + \mathbf{f} = 0, \quad (2.4)$$

with the Cauchy stress tensor  $\boldsymbol{\sigma}$ , which defines the state of the stress at a point inside a deformable material. In fluid dynamics it is common to split the tensor into a deviatoric part  $\boldsymbol{\sigma}^D$  and a pressure part  $p\mathbf{I}$ :

$$\boldsymbol{\sigma} = \boldsymbol{\sigma}^D - p\mathbf{I}, \quad (2.5)$$

where  $\mathbf{I}$  is the identity tensor and  $p = -\frac{1}{3} tr(\boldsymbol{\sigma})$  denotes the pressure. The volume force  $\mathbf{f}$  contains gravitation force, from the rotating Earth centrifugal force and Coriolis force. The Coriolis force can be neglected, since the glacier ice is flowing with slow velocities. The gravitational and centrifugal force are combined into the effective force of gravity  $\rho \mathbf{g}$ . The vector of the gravitational acceleration has the form of  $\mathbf{g} = (0, 0, -g)$ , with  $g = 9.81 \text{ m s}^{-2}$ . This leads to the Stokes equation:

$$div(\boldsymbol{\sigma} - p\mathbf{I}) = -\rho \mathbf{g} \quad (2.6)$$

### 2.1.3. Enthalpy formulation

For the description of the energy balance the approach by Aschwanden et al. (2012) is followed in order to determine cold, temperate ice and water with the same equation. As

well as above the most important equation are shown from the papers by Aschwanden et al. (2012) and Kleiner et al. (2015). In thermodynamics literature (Moran and Shapiro (2006)) the specific enthalpy  $E$  is defined as  $E = U + p/\rho$ , where  $U$  is the specific internal energy and  $p$  the pressure. Since the work associated with changing the volume of the material is not included, it can be set  $E = U$  with the SI unit  $J kg^{-1}$ . In the following the enthalpy is described as functions of temperature  $T$  depending on the phase of the material. For cold ice, below the pressure melting point ( $T_{pmp}$ ), the specific enthalpy of ice  $E_i$  is defined as:

$$E_i = \int_{T_0}^T C_i(T) dT, \quad (2.7)$$

where  $C_i(T)$  is the heat capacity of ice and  $T_0$  is the reference temperature. If this temperature is lower than all modelled temperatures the enthalpy will be always positive. The specific enthalpy of liquid water  $E_w$  reads as:

$$E_w = \int_{T_0}^{T_{pmp}(p)} C_i(T) dT + L + \int_{T_{pmp}(p)}^T C_w(T) dT, \quad (2.8)$$

where  $C_w(T)$  is the heat capacity of water and  $L$  the latent heat of fusion. A further advantage of the enthalpy formulation is that temperate ice ( $T = T_{pmp}$ ) can be described with a resulting water content ( $\omega$ ). This leads in case of temperature below the pressure melting point ( $T < T_{pmp}$ ) to a water content of zero ( $\omega = 0$ ), or for temperature at the pressure melting point ( $T = T_{pmp}$ ) to water content between zero and 100% ( $0 \leq \omega \leq 1$ ). The specific enthalpy of mixture, including cold ice, temperate ice and liquid water reads as:

$$E = E(T, \omega, p) = (1 - \omega) \cdot E_i(T) + \omega E_w(T, p). \quad (2.9)$$

These leads to two cases:

$$E = \begin{cases} E_i(T), & T < T_{pmp}(p) \\ E_s(p) + \omega L, & T = T_{pmp}(p) \text{ and } 0 \leq \omega \leq 1 \end{cases}. \quad (2.10)$$

There are the following transfer rules for temperature and water content to enthalpy:

$$E(T, \omega, p) = \begin{cases} c_i(T - T_{ref}), & \text{if } E < E_{pmp} \\ E_{pmp} + \omega L, & \text{if } E \geq E_{pmp} \end{cases} \quad (2.11)$$

#### 2.1.4. Enthalpy balance

The enthalpy balance for ice reads (Aschwanden et al., 2012):

$$\frac{\partial(\rho_i E_i)}{\partial t} = -\nabla \cdot (\rho_i E_i \mathbf{v} + \mathbf{q}_i) + Q_i - \sum_w, \quad (2.12)$$

and similar for liquid water:

$$\frac{\partial(\rho_w E_w)}{\partial t} = -\nabla \cdot (\rho_w E_w \mathbf{v} + \mathbf{q}_w) + Q_w + \sum_w, \quad (2.13)$$

where  $\sum_w$  is the enthalpy exchange rate between components,  $Q_i$  and  $Q_w$  are the dissipation heating rates. The advective and non-advective enthalpy fluxes of the ice component are  $\rho_i E_i \mathbf{v}$  and  $\mathbf{q}_i$ , respectively and same for the liquid component. From equ. 2.12 and 2.13 leads to the balance for the total enthalpy flux:

$$\rho \frac{d(E)}{d t} = -\nabla \cdot \mathbf{q} + Q, \quad (2.14)$$

where  $\mathbf{q} = \mathbf{q}_i + \mathbf{q}_w$ . The rate,  $Q$ , at which dissipation of strain releases heat into the mixture is:

$$Q = tr(\boldsymbol{\sigma} \cdot \boldsymbol{\sigma}^D) \quad (2.15)$$

## 2.2. Constitutive equations and rheology of ice

The balance equations, derived above, are principles. They need determining equations in order to represent specific materials. These constitutive equations close the above balance equations since there are 3 sets of equations from mass balance and momentum balance but 6 unknowns (Pressure, velocity and stress).

### 2.2.1. Incompressible Newtonian flow

Any isotropic fluid can be described by the relation between the deviatoric viscous stresses ( $\boldsymbol{\sigma}^D$ ) and the strain rates tensor ( $\dot{\boldsymbol{\epsilon}}$ ).

$$\boldsymbol{\sigma}^D = 2\eta \dot{\boldsymbol{\epsilon}}, \quad (2.16)$$

where  $\eta$  is the viscosity and the strain rate tensor  $\dot{\boldsymbol{\epsilon}}$ , written in component form:

$$\dot{\epsilon}_{ij} = \frac{1}{2} \left( \frac{\partial u_i}{\partial x_j} + \frac{\partial u_j}{\partial x_i} \right).$$

If the viscosity is constant, which is the case for liquid water at given temperature, than the stress is linear proportional to the strain rate. Fluids, which have a linear relationship between strain rate and stress, are called Newtonian fluids.

### 2.2.2. Incompressible Non-Newtonian fluids and the rheology of ice

In glaciers ice does not occur as on single crystal. It is rather build up a great assemblage of crystals (so called grains or crystallites). The sizes are on a millimetre to centimetre scale. On an average the orientation of the single crystals are randomly distributed, so

that an isotropic behaviour is assumed for glacier ice. If a block of ice is sheared with a constant stress ( $\tau$ ) a shear angle ( $\gamma$ ) will develop as show in Fig. 2.1. The angle measured over time gives a creep curve (shown in Fig. 2.1). First the ice responds elastic on applied force followed by a phase called primary creep, where the shear rate ( $\dot{\gamma}$ ) decrease with time. At one point the minimum shear rate is reached and stays constant (the secondary creep phase). Before the last phase the tertiary creep sets in, which is the case at high homologous temperatures and long time scales, an acceleration phase can be recognized (Greve and Blatter, 2009). These phases can be attributed to dynamic recrystallization of the crystallites.

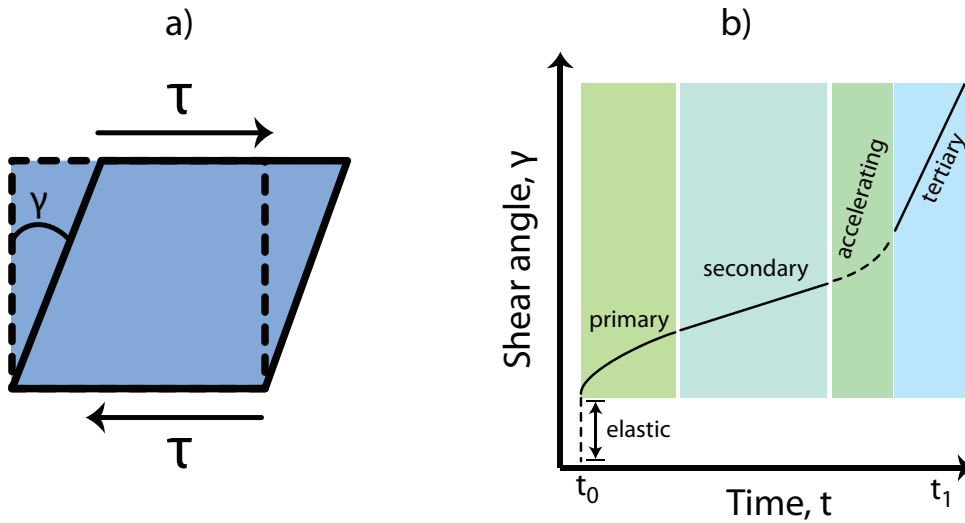


Figure 2.1.: a) a block of ice is sheared (in a simple shear form) showing the resulting shear angle  $\gamma$ ,  
 b) Diagram of the evolution of the shear angle over time, modified after Greve and Blatter (2009).

### 2.2.3. Glen's flow law

For glacier ice laboratory and field data have shown that the connection between strain rate and stress depends on a power law (Glen, 1955). The generalized form by Nye (1957) reads as:

$$\dot{\epsilon}_{ij} = E A \tau_e^{Dn-1} \tau_{ij}^D, \quad (2.17)$$

where ( $\tau_e^D$ ) is the effective deviatoric stress, the second invariant of the deviatoric stress tensor. The factor  $A$  is called the *flow rate factor* and is dependent on temperature and water content ( $A = A(T, \omega)$ ).  $E$  is called the *enhancement factor* and parameterizes other physical contributions, like fractures or impurities. The power law exponent  $n$  is set to 3 by convention (Cuffey and Paterson, 2010). In the model  $A$  and  $E$  are kept constant for simplicity reasons. The inverse form of Glen's law reads as:

$$\tau^D = 2 \eta \dot{\epsilon} \quad \text{with} \quad \eta(\dot{\epsilon}) = \frac{1}{2} (E A)^{-\frac{1}{n}} \dot{\epsilon}^{\frac{1-n}{n}}, \quad (2.18)$$

with the effective strain rate  $\dot{\epsilon}_e = \sqrt{\frac{1}{2} \text{tr} \dot{\epsilon}^2}$ . Ice behaves like a Non-Newtonian fluid as the relation between stress and strain is non linear and the viscosity is dependent on the effective strain rate  $\eta = \eta(T, \dot{\epsilon}_e)$ . The viscosity of ice ranges around  $10^{13} \text{ Pa s}$  (at  $T = 0^\circ\text{C}$  and  $\tau_e = 100 \text{ kPa}$ ) to  $10^{17} \text{ Pa s}$  (at  $T = -20^\circ\text{C}$  and  $\tau_e \approx 10 \text{ kPa}$ ). In comparison motor oil has a viscosity of  $0.1 \text{ Pa s}$  and the Earth's mantel  $10^{21} \text{ Pa s}$  (Greve and Blatter, 2009).

### 2.3. Boundary conditions

The previously derived balance equations are only applicable if the thermodynamic field is sufficiently smooth and thus continuously differentiable. This assumption is not valid on the surfaces of the model and the surroundings. These interfaces, which experience a discontinuity in a physical quantity, are called singular surfaces. Jump conditions or boundary conditions have to be formulated in order to close the equations. There are three types of boundary conditions. The Neumann boundary condition prescribes the derivative of a quantity at the interface. If the value of the field quantity is set to a certain value, it is called a Dirichlet boundary condition. There is also a third type of condition, which is a mixture of the both and is called Robin condition. Four boundary conditions are need for the description of the model. They are the boundary condition for the boundaries between ice/atmosphere, ice/water, water/lithosphere and ice/ice. They are described in the following sections and are schematically illustrated in Fig. 2.2.

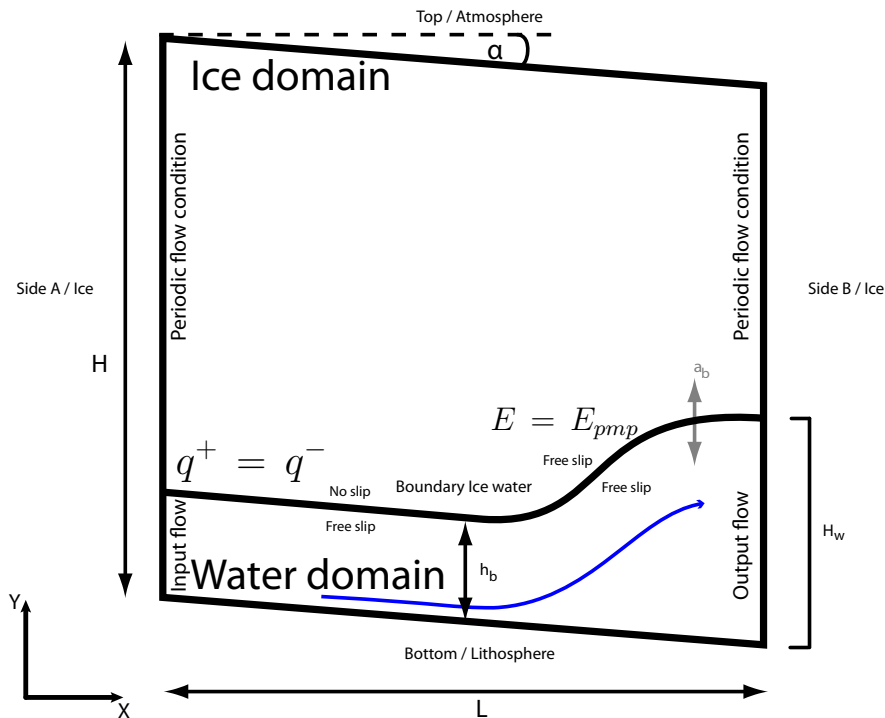


Figure 2.2.: Schematic drawing of the geometry setup with implemented boundary condition switches. Please not that the x-axis is pointing horizontally and y-axis vertically. This is against convention but results from Comsol interior labling.

### 2.3.1. Ice surface

The boundary between ice and atmosphere is regarded to be a singular surface and its implicit form can be written as followed:

$$F_s(\mathbf{x}, t) = z - z_s = z - h(x, y, t) = 0, \quad (2.19)$$

where  $z_s = h(x, y, t)$  is the position of the ice surface. The kinematic boundary condition reads as:

$$\frac{\partial z_s}{\partial t} + v_x \frac{\partial z_s}{\partial x} + v_y \frac{\partial z_s}{\partial y} + v_z = N_s a_s^\perp, \quad (2.20)$$

where the  $a_s^\perp$  is the accumulation perpendicular to the surface and  $N_s$  is the gradient norm:

$$N_s = |\nabla F_s| = \left( 1 + \left( \frac{\partial z_s}{\partial x} \right)^2 \right)^{\frac{1}{2}}. \quad (2.21)$$

Since the stress applied by the atmosphere and wind on the surface are very small in comparison to normal stresses ice and thus negligible. The ice/atmosphere boundary can be seen as a traction free surface:

$$\mathbf{t} \cdot \mathbf{n} = 0. \quad (2.22)$$

This is called the dynamic boundary condition. The thermodynamic boundary condition is described by a Dirichlet condition. The enthalpy is prescribed by a mean annual value  $E_s(x, y, t)$ :

$$E = E_s(x, y, t) \quad (2.23)$$

### 2.3.2. Ice base

Analogous to the singular surface at the ice/atmosphere boundary the kinematic boundary condition for the ice base ( $F_b(\mathbf{x}, t) = z - z_b = z - h(x, y, t) = 0$ ) can be derived and reads:

$$\frac{\partial z_b}{\partial t} + v_x \frac{\partial z_b}{\partial x} + v_y \frac{\partial z_b}{\partial y} + v_z = N_b a_b^\perp, \quad (2.24)$$

where  $z_b$  is the height of the basal interface and  $N_b$  is the norm of the normal vector.

$$N_b = |\text{grad } F_b| = \left( 1 + \left( \frac{\partial z_b}{\partial x} \right)^2 \right)^{\frac{1}{2}} \quad (2.25)$$

In the case that water is present at the base, the geothermal heat flux ( $q_{geo}$ ) enters into the water domain. In the case of ice at the base, the thermal conductivity parameter ( $K_j$ ) changes to the one of ice. Thermodynamic boundary at the boundary between water and lithosphere is therefore:

$$-K_j \cdot \nabla E \cdot \mathbf{n}_b = q_{geo} \text{ with } j = [w, i]. \quad (2.26)$$

### 2.3.3. Ice water interface

Since this thesis deals with subglacial drainage systems and in order to evolve them melting and refreezing plays an enormous role. The basal melt rate ( $a_b$ ) is calculated by the difference of heat fluxes at the interface (see equ. 2.29).

In the following it has to be distinguished between the different conditions, which can occur underneath an ice sheet. The boundary conditions are linked to the presence of water and if the ice is temperate or not.

For the thermodynamic boundary condition there is a decision chart given by Aschwanden et al. (2012), which is adapted for this model. These decisions read as followed:

**Cold base (dry):** The glacier is cold at the base and/or the water layer is smaller or equal the minimum water thickness (plus a small value  $\epsilon$  for numerical stability) ( $(H_w \leq hb + \epsilon \wedge E < E_{pmp}) \vee (H_w \leq hb + \epsilon \wedge E \geq E_{pmp})$ ), then a Neumann boundary condition holds and sets fluxes on both sides equal:

$$-\mathbf{n}^+ \cdot (k \nabla E)^+ = -\mathbf{n}^- \cdot (k \nabla E)^- \quad (2.27)$$

$$E^+ = E^-, \quad (2.28)$$

where the superscript  $+$  and  $-$  define respectively one side of a boundary. Here it can be referred to ice side  $+$  and water side  $-$ .

**Cold or temperate base with water:** If the water layer is larger than the original minimum water thickness ( $H_w > hb + \epsilon \wedge E < E_{pmp}) \vee (H_w > hb + \epsilon \wedge E \geq E_{pmp})$ , the conditions at the interface change to a Dirichlet condition  $T = T_{pmp}$ . Therefore the interface condition represents a third type condition, which is updated at every timestep. Since the temperature is kept constant at the boundary, all exceeding energy is converted into melting. The melt rate is calculated by difference of heat fluxes at the boundary between ice and water  $\partial\Omega_{i-w}$  and reads as followed (the unit is  $\text{mm a}^{-1}$  in ice equivalent):

$$a_b = -\frac{(q_i - q_w) \mathbf{n}_b}{L \cdot \rho_i}, \quad (2.29)$$

where  $L$  is the latent heat of fusion  $\rho_i$  the density of ice. The terms  $q_i$  and  $q_w$  are the conductive heat fluxes of ice and water, respectively. They result from the enthalpy version of Fourier's law and are calculated by:

$$q_j = -K_j \nabla E, \quad (2.30)$$

where  $j = i, w$  indexing ice or water and  $K_j = k_j/c_j$  is the thermal conductivity in enthalpy form.

Further the flow conditions have to change for the ice. The boundary condition switches from a non-slip condition to a slip condition. It is achieved by manipulating the friction coefficient at the boundary. As soon as the water thickness rises above the original limits the friction coefficient ( $\beta^2$ ) decreases significantly. In case of a frozen bed the friction coefficient is infinitely large and hence no sliding occurs. The friction parameter ( $\beta^2 [Pa a m^{-1}]$ ) is related to the basal drag  $\tau_b$  (sum of all basal resistance at the base) and the basal velocity ( $\mathbf{v}_b$ ) (Pattyn, 2010) by

$$\tau_b = \beta^2 \cdot \mathbf{v}_b \quad (2.31)$$

#### 2.3.4. Lateral boundaries

Since the model is representing the interior of an ice sheet, the lateral boundaries have to represent these conditions. Therefore the boundary conditions are chosen to simulate the as if multiple copies of itself would surround the domain. Since the domain lateral boundaries are fixed in space, a kinematic boundary condition can be omitted. The dynamic boundary conditions are chosen to represent a periodic wall and read as:

$$\mathbf{v}^+ = \mathbf{v}^- \quad (2.32)$$

$$p^+ = p^-, \quad (2.33)$$

where  $\mathbf{v}^+$  and  $\mathbf{v}^-$  are the velocities of the destination and source boundary, respectively and  $p^+$  and  $p^-$  the pressure of the destination and source boundary, respectively.

For the thermodynamic boundary condition at the lateral boundaries an insulating condition is chosen, so that there is no enthalpy gradient over the interface. That is in contradiction to the cyclic environment proposed above. Nevertheless it brings a better numerical stability into the model. Thus the thermal insulation reads as:

$$-\mathbf{n} \cdot (-k \nabla E) = 0 \quad (2.34)$$



## 3. The numerical model

### 3.1. Implementation

The implementation of the model into the commercial software COMSOL Multiphysics<sup>®</sup> is shown in this Chapter. This program offers the ability to solve Partial Differential Equations (PDE), like the heat transfer equation or the Navier-Stokes equation (see Chapter 2), on the numerical approach of the Finite Element Method. COMSOL Multiphysics<sup>®</sup> can be used via a Graphical User Interface (GUI), a live-link via Matlab<sup>®</sup> or via JAVA API. In the following the use of the GUI will be described in detail. The GUI enables a quick and easy handling of models and their implementation. Since, COMSOL Multiphysics<sup>®</sup> is a commercial software is not possible to see into the source code and this is a disadvantage in some cases for detailed manipulation in the model.

The GUI (see fig 3.1) is divided into three main parts the *Model Builder*, the *Node properties* and *Graphics*. The model is created by successively adding nodes (branches) in the *model builder tree* in the *Model Builder* section. By default the branches *Global Definitions*, *Model*, *Study* and *Results* are pre-set. The branch *Global Definitions* is used to define global valid parameters, shown in Table 3.1. If not mentioned over wise, these parameters and variables are used as default values for the model setups.

The *Model builder tree* is subdivided into several subbranches/subnodes. Here the nodes *Definitions*, *Geometry* and *Mesh* are set as default. It is a strength of Comsol to add pre-described PDE (the so called Physics) to the model at this point. The Physics nodes *Heat transfer in Fluids*, *Laminar Flow 1 and 2* and *Moving Mesh* were added to the model tree. In the node *Definitions* variables can be defined and further selections of certain areas of the model geometry can be set, which improves the later handling.

#### 3.1.1. Geometry

The geometry of the model defines the domain, where the PDEs are solved. The geometry node offers the ability to design all possible shape. This can be achieved by assembling different geometry object like circles, rectangle, lines or spline curves. These objects can be transformed in a more complex geometry by operators like union, split, difference and intersect. It also possible to load externally built geometries by a Computer Aided Design Program into Comsol (only possible with extended licence).

For subglacial water models a rather simple geometry is chosen, in order to represent a segment of an ice sheet. The shape is approximated by a two dimensional square ('ice

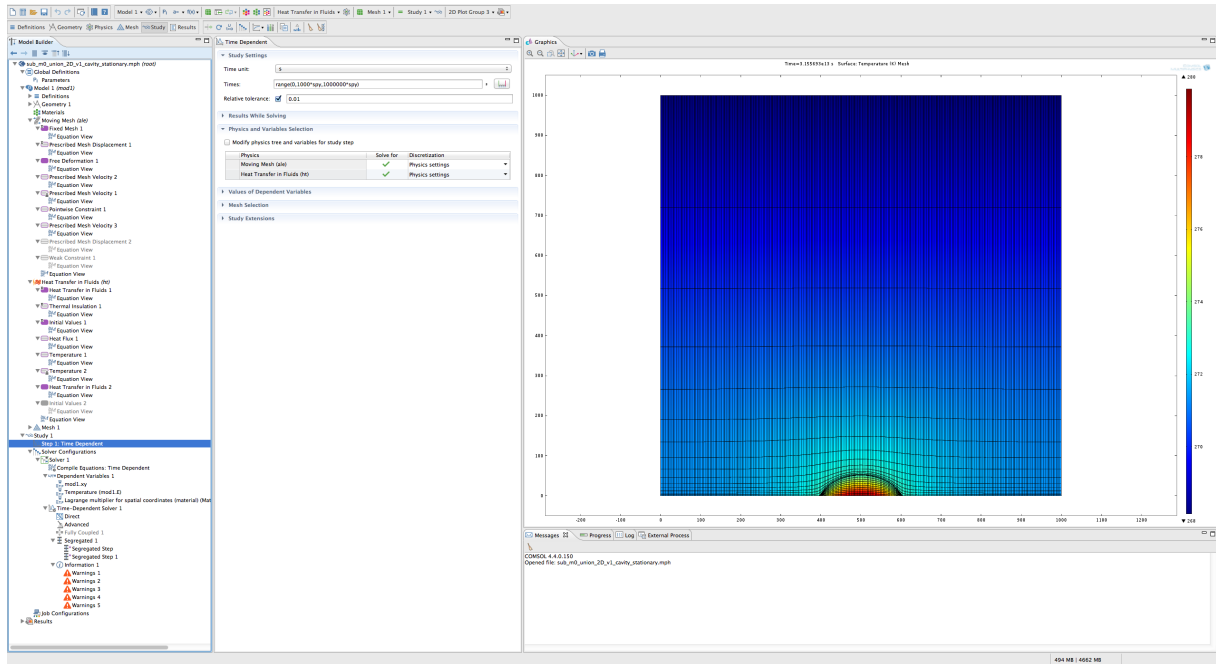
Figure 3.1.: Screenshot of Comsol Multiphysics<sup>®</sup> GUI

Table 3.1.: Default physical global parameters

name	expression	unit	description
rho_ice	910	kg/m <sup>3</sup>	Density of ice
rho_water	1000	kg/m <sup>3</sup>	Density of water
g	9.81	m/s <sup>2</sup>	gravity acceleration
spy	31556926		seconds per year
L_f	339000	J/kg	Latent heat of fusion
q_geo	42	mW/m <sup>2</sup>	geothermal heat flux
n	3		Exponent in Glen's Flow law
k_ice	2.1	W/m/K	thermal conductivity of ice
cp_ice	2009	J/kg/K	specific heat capacity of ice
cp_water	4216.278	J/kg/K	constant specific heat capacity of water at T <sub>0</sub>
k_water	0.556	W/m/K	constant thermal conductivity of water at T <sub>0</sub>

cube') with the height  $H$  and length  $L$  (all geometry linked parameters and variables are found in Table 3.2). This block is divided into two subdomains like shown in schematic fig 2.2. The creation of two domains is necessary due to topological reasons. Since the water is non existing at the start of the simulation it still needs an object to evolve itself. Otherwise the water domain would be generated out of nothing, which is not possible. The two sub domains are built as followed. The ice domain is overlaying the water domain and has an original thickness of  $h_t$ . Whereas, the water domain has a initial thickness of  $h_b$ . These values were chosen in order to have the lowest possible thickness for the water domain, which is still in the building tolerances. Moreover, it fulfils the topology

requirements and has the least effect on the starting conditions of the numerical model. During the simulation run the water domain may evolve and change geometry according to the melt rate ( $a_b$ ) at the boundary between ice and water. Further the domains have a slope with the angle  $\alpha$ . Creating the slope and the internal boundary between ice and water is achieved by inserting a line according to the function  $Z_{top}$ ,  $Z_{inter}$ ,  $Z_{bottom}$  in order to represent the boundaries ice/atmosphere, internal ice/water and ice/lithosphere respectively. Since all parameters are globally defined, they can be changed according to the model setups. Further, please note that the axis labelling is against convention. The x-axis is pointing in horizontal and the y-axis in vertical direction.

Table 3.2.: Default geometry parameters and variables

name	expression	unit	description
L	1000	m	Length of block
H	1000	m	Height of block
$\alpha$	0...0.1	°	Angle of the slope
slope	$\tan(\alpha)$		Gradient of the slope
$h_b$	3	mm	Initial height of water domain
$h_t$	$H - h_b$	m	Initial height of ice domain
$Z_{top}$	$-\text{slope} \cdot x + H$	m	Function of top boundary
$Z_{inter}$	$-\text{slope} \cdot x + h_b$	m	Function of internal boundary
$Z_{bottom}$	$-\text{slope} \cdot x$	m	Function of bottom boundary

### 3.1.2. Switch values

As mentioned above the water domain is evolving in time. This leads for example to a change in the boundary condition at  $\partial\Omega_{i-w}$  as shown in Chapter 2.3.3. Switching condition during the simulation requires an additional processing step during calculations. This change is enabled by a parameter switch. The so called `liquid` parameter is a logical parameter indicating if the water domain is larger than the initial height of  $h_b$ .

$$\text{liquid} = \begin{cases} 1 & , H_w > h_b \\ 0 & , H_w \leq h_b \end{cases}, \quad (3.1)$$

where  $H_w$  is the thickness of the water domain. This parameter enables to control changes of other physical parameters and initialisation of processes. It

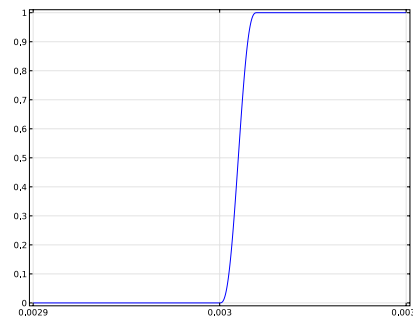


Figure 3.2.: Smoothed Heaviside function by the Comsol build in function `flc2hs` of the liquid parameter smoothed over  $10^{-5}$  m

triggers the switch of the Neumann to the Dirichlet condition at the internal boundary, the change from the physical properties of ice to water in the water domain and the start of the water flow. The explicit use is described in the sections below when the `liquid` switch is of need. Since numerical models do not cope well with hash changes the `liquid` parameter has to be smoothed. This is achieved by applying a smoothed Heaviside function the `liquid` parameter. Comsol offers the so called `flc2hs` function which is a built in smoothed Heaviside function with a continuous second derivative without overshoot (COMSOL Inc, 2015). In fig 3.2 the smoothing of `liquid` is shown with a smoothing over  $10^{-5}$  m. The implementation is done via adding a variable branch under the *Definition* branch in to Comsol GUI.

### 3.1.3. Mesh

The mesh is the discretisation of the domain, which enables solving the PDEs at the nodes. Therefore the mesh has a huge importance for the model. It has influence on the stabilization, convergence and computational cost. The mesh is chosen to have a fine resolution in the water domain, since the gradients are larger here due to the fast flowing water.

The meshing created with the Comsol built-in meshing operator `Mapped`, which is for building rectangular mesh elements. In order to define the amount of elements `Distributions` are defined on the domain borders. The water domain has 10 elements in  $y$  directions and 250 in  $x$  directions, creating 2500 elements in the water domain with a height of 0.3 mm and a width of 4 m. The ice domain has the same number of elements in  $x$  directions and 25 in  $y$  direction. This creates 6250 mesh elements. They are not equal sized like in the water domain but increase in size in  $y$  directions with a factor of 0.01, since smaller elements are needed at the boundary between ice and water. In the region near the boundary between ice and atmosphere no huge changes are expected and therefore not as many elements are needed.

### 3.1.4. Arbitrary Lagrangian Method (ALE), Moving Mesh

In order account for an evolving water column the internal boundary has to move according to the melt rate at the interface between water and ice. The melt rate  $a_b$  in ice equivalent is calculated according to equ. 2.29. The melt rate  $a_b$  is applied on the boundary and is constrained by the minimal thickness of the water layer ( $h_b$ ) and the direction of the melt rate. Therefore the moving mesh velocity  $v_{a_b}$  reads:

$$\mathbf{v}_{a_b} = \begin{cases} 0 & , H_w < h_b \wedge a_b \leq 0 \\ a_b \cdot \mathbf{n} & , H_w \geq h_b \wedge a_b > 0 \end{cases} , \quad (3.2)$$

If the  $\partial\Omega_{i-w}$  reaches the minimum thickness  $h_b$  then  $\partial\Omega_{i-w}$  is constrained by:

$$\partial\Omega_{i-w}(y) = \begin{cases} \partial\Omega_{i-w}(y) & , H_w > h_b \vee a_b > 0 \\ \partial\Omega_{i-w}(h_b) & , H_w \leq h_b \vee a_b \leq 0 \end{cases} \quad (3.3)$$

This constraint avoids penetrations of the ice domain into water domain and the lithosphere. Moreover, it triggers the `liquid` parameter, which controls several other switches as mentioned above.

The calculation of the new mesh coordinates  $x$ ,  $y$  is done with linear mesh elements. Since the input velocity (melt rate  $v_{a_b}$ ) is not always smooth across the elements, the mesh is smoothed with a *Laplace* algorithm.

The deformation of the mesh results from the calculated melt rate at the boundary between ice and water ( $\partial\Omega_{i-w}$ ). In Comsol the node *Fixed Mesh* and *Prescribed Mesh Displacement* are default in the *ALE* branch. In order to allow mesh movement the *Free Deformation* has to be added to the branch. Since only the boundary  $\partial\Omega_{i-w}$  shall move free, it is necessary to set the movement of the other walls to zero with a *Predefined Mesh velocity* node. This includes the boundaries top, bottom and sides (see Fig. 2.2).

A second *Predefined Mesh velocity* node is added to the branch in order to apply the melt rate on the internal boundary  $\partial\Omega_{i-w}$  according to equations 3.2. The no penetration condition (equ. 3.3), are implemented by a *Pointwise constraint* node. This prohibits the boundary  $\partial\Omega_{i-w}$  to lower itself beneath the minimum height of  $h_b$ .

### 3.1.5. Heat transfer in fluids

The implementation of the heat flux in the model is done via the Physics node *Heat transfer in fluids*. Here the enthalpy  $E$  is solved in the domains. As described in the Chapter, 2.1.3 and 2.1.4, transformation rules are needed to convert the enthalpy into temperature, which is the more comprehensible physical quantity for glaciologist and marine geologists. These transformation rules are implemented under a variable node in the *Local Definitions* and listed in Table 3.3. Furthermore, the parameters for the boundary conditions, the thermal conductivity of ice and water and the calculation of the temperature / enthalpy at the pressure melting point ( $T_{pmp}$  and  $E_{pmp}$ , respectively) are listed in the same table.

The general picture of the model regarding the heat transfer is that there is a heat source at the bottom and a constant temperature at the top. Furthermore, the two domains have a different parameters resulting from the different phases in

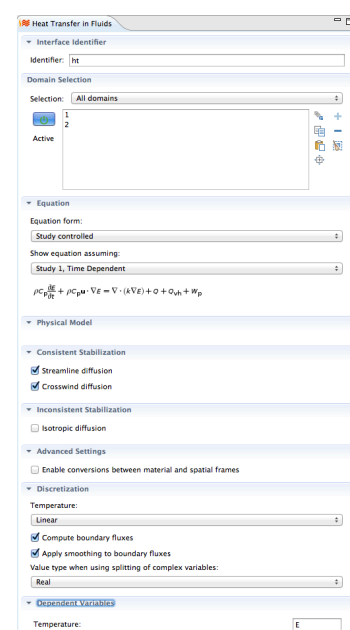


Figure 3.3.: Top branch of the *Heat transfer* node

Table 3.3.: Heat transfer parameters and variables

name	expression	unit	description
T_ref	223.15	[K]	Reference Temperature
T_0	273.15	[K]	Melting point of water under normal pressure
T_top	268.15	[K]	Temperature at the top
E_start	$cp\_ice*(T\_top-T\_ref)$	[J/kg/K]	starting Enthalpy
my_p	$\rho_{ice}*(H-y)*g$		pressure
beta	$7.9e-8$	[K/Pa]	Clausious-Clapeyron constant
T_pmp	$T_0-beta*my\_p$		Temperature at pressure melting point
E_pmp	$cp\_ice*(T\_pmp-T\_ref)$	[J/kg/K]	enthalpy at Pressure melting point
K_0	$k\_ice/cp\_ice/10$	[kg/J*K]	moisture mass diffusivity, conductivity of temperate ice
K_c	$k\_ice/cp\_ice$	[kg/J*K]	Conductivity of cold ice
K_water	$k\_water/cp\_water$	[kg/J*K]	constant thermal conductivity of water
T	$if(E < E\_pmp, E/cp\_ice+T\_ref, T\_pmp)$	[K]	Temperature
omega	$if(E \geq E\_pmp, (E-E\_pmp)/L\_f, 0)$		water content

the model. In order to create such a model the following adjustments in the *Heat transfer* node have to be made:

- The topbranch *Heat transfer in fluids* is for general settings (compare Fig. 3.3 ). The domains one and two (all domains) are the regions where the PDE of the heat transfer is solved. They are set in the window domain settings. Under equations the equation type is chosen to be study dependent. In our case this is a time dependent form. In contrast if the stationary is chosen, the time dependent part would be set to zero ( $c_p \rho \partial E / \partial t = 0$ ). Furthermore, *Streamline* and *Crosswind* diffusion are enabled as stabilization techniques. They avoid numerical instability caused by temperature advection. The *streamline* stabilisations adds numerical diffusion in streamline direction (Codina, 1998), whereas the *crosswind* diffusion acts in orthogonal direction to the streamline (Hauke and Hughes, 1998). Under the section *Discretization* linear elements are chosen for the FEM shape functions. The option *Compute boundary fluxes* and *Apply smoothing of boundary fluxes* is enabled,

which is of major importance. These fluxes contribute to the calculation of the melt rate. The section *Dependent variables* is for the naming the variable, here  $E$ .

- The first subnode is the *Heat transfer in fluids 1*. The parameters of the ice domain (domain 2 in Comsol) are defined here. Comsol solves the following equation for the heat transfer:

$$\rho c_p \frac{\partial E}{\partial t} + \rho c_p \mathbf{u} \cdot \nabla E = \nabla \cdot (k \nabla E) + Q + Q_{vh} + w_p, \quad (3.4)$$

where  $\rho$ ,  $c_p$  and  $k$  can be set in the node window and are the density, the heat capacity at constant pressure and the thermal conductivity respectively of the fluid. The terms  $w_p$ ,  $Q_{vh}$  are Comsol interior source terms and are set to zero. The term  $Q$  is given by equ. 2.15. The equation has to be modified in order to resemble the enthalpy formulation. Therefore, the conductivity of cold ice ( $K_c$  see Table 3.3 ( $K_c = k_c/c_p$ )) is inserted in the place of the thermal conductivity, for the heat capacity is one and for the rho is set to be the density of ice ( $\rho_{ice}$ ). The model will simulate the change of enthalpy according to the flow. Hence, the heat transfer is coupled with the laminar flow (described below) under the rubric *Model inputs*. The corresponding laminar flow 1 is chosen as input variables for the velocity field  $\mathbf{u}$  and the absolute pressure  $p$ .

- In the above setting the implementation of the heat transfer for the ice domain is described. Corresponding the heat transfer is implemented into the water domain. For that reason, a second *Heat transfer in fluids* (subbranch) is added to the physics branch. This one is only valid for the water domain (domain 1 in Comsol). Here the same equ. 3.4 is solved for the water domain with all interior source terms set to zero. Similar to the above described the conductivity of water ( $K_{water}$ ), the density of water ( $\rho_{water}$ ) and the thermal conductivity of water equal one are introduced into model. Like above, the water flow is linked to the heat transfer model via the rubric *Model inputs* and here chose the laminar flow 2.
- Numerical models need a initial value as we solve an initial- and boundary value problem. This value should be a good guess, representing the logical physical field corresponding to the later values. Thus an incorrect choice can lead to non-convergence of a model. Here, in the subnode *Initial values* the enthalpy  $E_{start}$  is chosen to be the starting value for the enthalpy calculation in the stationary solver.

**Boundaries** The boundary conditions which are described already in Chapter 2 are here implemented as followed in the model. It needs three boundary conditions: the ice surface (boundary ice/atmosphere), the water/ice base (ice or water/lithosphere) and the sides (ice/ice).

- Ice surface: The temperature is defined at the top of the model, which in this case the enthalpy, to be a constant value  $T_{top}$ , transformed into  $E_{start}$  (see Table 3.3). This resembles a Dirichlet-boundary condition and is implemented via the subnode *Temperature*.
- Base: The boundary between water domain and lithosphere is described as a Neumann boundary condition. The geothermal heat flux ( $q_{geo}$ ) is prescribed here. This is implemented via the Comsol subnode *Heat flux*.
- Sides: The model is supposed to represent an interior of an ice sheet. Therefore, the sides should represent as if the model would be surrounded by an infinite number of itself. This would be accomplished by periodic boundary condition. Hence, everything, which flows out of the model, flows in on the opposite side. This type of boundary condition leads unfortunately to non-convergence of the model. Therefore, a thermal insulation boundary condition is implemented, which is a default setting by Comsol. The heat flux is set to zero at the sides, so that  $-\mathbf{n} \cdot (-k\nabla E) = 0$ .
- Internal Boundary: The boundary between ice and water experiences a switch during the calculation. During the period that `liquid` is equal to one, the boundary will be treated as a von Neumann boundary. The fluxes on both side are equal  $q_i = q_w$ . As soon as `liquid` increases to one the boundary condition flips to a Dirichlet condition and prescribes the enthalpy to be at pressure melting point  $E = E_{pmp}$ . This switch is implemented via the subnode *Temperature*.  $E_{pmp}$  is set in the field for temperature. In order to introduce the switch the equation settings have to be manipulated. Here the constrain setting is multiplied by a combination of parameter as shown below in order to assure the Dirichlet condition to be full filled during an increased water thickness and limited only to the region where  $E_{pmp}$  is already reached.

$$bc = \begin{cases} 0 & , \text{if } liquid < 1 \& E < E_{pmp} \\ 1 & , \text{if } liquid = 1 \& E \geq E_{pmp} \vee liquid = 1 \& E < E_{pmp} \end{cases} \quad (3.5)$$

### 3.1.6. Laminar flow 1 + 2

The flow of the model is introduced via the physics node *Laminar flow*. As mentioned in the introduction, this thesis includes as well turbulent water flow, hence the title of seams to be a contradiction. This obstacle can be overcome, since the *Laminar flow* includes the Navier-Stokes equation and is therefore able to model turbulent fluxes. For better handling the Navier-Stokes equation is implemented via two separated Comsol physics nodes, the so called *Laminar flow 1* and *2* (corresponding to the ice and the water domain, respectively). The Navier-Stokes equation is able to model the high viscous flow of ice and turbulent flow of water. In the ice domain the high viscosity of ice ( $\approx 10^{14} Pa s$ ), hence a low Reynolds number, will minimize the effect of turbulent part in Navier-Stokes equation ( $\mathbf{v}\nabla\mathbf{v} \approx 0$ )

. Whereas, the low viscous water flow in the water domain will allow turbulent fluxes. It solves for the variables  $u, v, p$  ( $v_x^i, v_y^i, p^i$ ), the velocity and the pressure of the ice flow and  $u_2, v_2, p_2$  ( $v_x^w, v_y^w, p^w$ ), the velocity and the pressure of the water flow. In order to avoid confusion, as mentioned above, the  $x$  and  $y$  subscript denotes the horizontal and vertical direction. All other variables and parameters necessary for the *Laminar flow* are set in Table 3.1 and Table 3.4 In the following the two *Laminar flow* nodes will be described.

### 3.1.6.1. Laminar flow 1, ice flow

#### Fluid properties

- Laminar flow 1, ice flow: Similar to the physics node *Heat transfer* the first node is the top branch *Laminar flow, ice flow*. Here the Navier-Stokes equations is displayed, the PDE which is solved for. Further, the ice domain (domain 2) is chosen to be the region, where the PDE is valid. Under Physical model rubric the flow type is set to be incompressible since ice is assumed to be incompressible. Like in the *Heat transfer* branch the model needs a specify the discretisation of the PDE. In turbulent flow modelling it is convenient to discretize the velocity part with quadratic elements (P2) and the pressure with linear elements (P1). This arises from the Babuška-Brezzi condition, which states that for numerical stability the basis functions for velocity have to an order higher than the basis functions for pressure. If the same basis functions are applied in order to decrease computational cost, the usage of a stabilization technique is necessary. In Comsol the *Streamline diffusion* (Galerkin Last Square) is activated in order to achieve the necessary stabilization.
- Fluid properties 1: This subnode is used for the implementation of the ice density ( $\rho_{ice}$ ) and the dynamic ice viscosity ( $\nu_{ice}$ ) of ice (see Table 3.1 and 3.4). The density of pure ice is  $917 \text{ kg m}^3$ , which is a bit more than our value, due to the fact that our lower value accounts for possible gas bubble intrusions. Moreover, a small value of  $10^{-25}$  and  $10^{-30}$  is added to the dynamic viscosity of ice  $\eta_{ice}$  and the effective deformation rate, respectively. These values are added to prevent that the initial effective deformation is no zero and thus the initial dynamic viscosity to be no zero. A starting dynamic viscosity would lead to unrealistic velocities and a non-convergence of the model.
- Initial values: Here, similar to *Heat transfer*, a initial velocity of zero and same for the pressure is implemented into the model via the *Initial value* subnode for the stationary solver.
- The Volume force, here the gravity, is given by the vector  $\mathbf{F} = (0, -\rho_{ice} \cdot g)^T$ , with  $g$  being the gravity acceleration and therefore, pointing in downward (in negative  $y$

direction see Fig. 2.2). It is implemented via the subnode *Volume forces* into the physics branch.

Table 3.4.: Laminar flow 1 + 2 variables and parameters

name	expression	unit	description
A	$10^{-16}$	$\text{Pa}^{-3} \text{ a}^{-1}$	Rate factor of ice
nu_ice	$0.5 \cdot A^{-1/n} \cdot (d + 10^{-30})^{((1-n)/n)}$	$\text{Pa s}$	dynamic viscosity of ice
d	$\text{sqrt}(0.5 \cdot u_x^2 + 0.25 \cdot (u_y + v_x)^2 + 10^{-25})$	$\text{s}^{-1}$	effective deformation rate
nu_water	$1.7 \cdot 10^{-3}$	$\text{Pa s}$	viscosity of water
u_input	$0.0001 \dots 10$	$\text{m s}^{-1}$	input velocity for water domain
beta2	50 and $\infty$	$\text{Pa a m}^{-1}$	friction coefficient
slip	$-\text{beta2} \cdot (u \cdot n_y + v \cdot n_x) \cdot \text{test}(u \cdot n_y + v \cdot n_x)$		slip value which implemented into slip equation

## Boundary conditions

- The ice surface to the atmosphere is tension free, when neglecting wind stress. This boundary condition is implemented via the subnode *Free Boundary*. The stresses are set to zero, symbolizing the tension free surface.
- The boundary between ice and water: Since this boundary applies for the water and the ice domain this boundary has two conditions at the same time depending on the domain. Therefore, the boundary has to be discussed in two steps. Here, it is focused at the ice side, the water side will be described in the section 3.1.6.2, the water flow implementation. When the ice is frozen to the ground, the basal velocity is zero. In this case a non - slip boundary condition applies to the ice. This can be added to the model by choosing a *Wall* as subnode and defining that *Wall* with a no slip condition. If the water domain turns to liquid the boundary condition has to change to a slip boundary condition. In order to achieve such a switch, a slip wall condition is implemented as if the ice could slide freely over the water domain. In

the same time the friction parameter is controlled, which regulates the sliding. This is implemented via the subnode *Wall*, and changing to *Slip* in the drop down menu. Further, in the equation settings of the wall the weak expression has to be edited and the friction depending on liquid is inserted into the equation settings. For the different experiments the friction coefficient ( $\beta^2$ ) is adapted to the necessary settings and is described in the experiments setups.

- The Sides of the ice domain are chosen to represent an interior of an ice sheet. Therefore, periodic boundary conditions are applied on the sides. So that everything which flow out of the model flow into the model on the over sides. Hence, it seams, as the model would be surrounded by an infinite number of itself.

### 3.1.6.2. Laminar flow 2, water flow

#### Fluid properties

- Laminar flow 2, water flow: Here in the top branch, similar to the above described physic nodes, the water domain (domain 1) is set to be the region, where the PDE is valid. Further the same proceder is applied for the discretization to set the same order of basis function for velocity and pressure and enable the streamline diffusion. The variables, which are solving for, are  $u_2, v_2, p_2$  in order to distinct them form the velocity and pressure variables in the ice domain.
- Fluid properties: Here the `liquid` switch is implemented as well. This leads to a switch from the density and viscosity of ice to density and viscosity of water (see Table 3.1). In the model a constant density and viscosity of water is applied for simplicity reason, since variance is small in the modelled temperature regime.
- Volume force: Corresponding to the ice domain the gravity as volume force would be  $\mathbf{F} = (0, -g \cdot \rho_{water})$ . Due numerical instabilities the volume force is set to zero and therefore, the input velocity only controls the water flow.

#### Boundary conditions

- Initial values: The boundary conditions applied on the water domain imply an input velocity and an output pressure. The value for the input velocity (`u_input` Table 3.4) is the initial value for the water domain.
- surface ice water and water lithosphere: The upper and lower wall surrounding the water domain have a slip boundary condition. This is implemented via adding the *Wall* subnode to the branch and switching to the wall condition to slip.

- The Sides have two different boundary condition, which require each other. On the left side of the inlet boundary condition is valid and on the right hand side operates the outlet boundary condition.
  - The **Inlet** boundary conditions is added to the branch and enables to chose a inlet velocity or pressure at the boundary. Here, the inlet velocity is set to `u_input` parameter (see Table 3.4) in the field for the normal velocity.
  - **Outlet:** In order that the inflowing water can exit the water domain, the outlet boundary is applied on the right side of the model. Here, the pressure at the outlet is put zero. This brings numerical stability into the model since defining the same outflow velocity brings a non-convergence. The implementation is done via the subnode *Outflow*.

### 3.1.7. Solver

In order to find a solution to the above implemented PDEs, Comsol Multiphysics<sup>©</sup> offers a variety of solvers. They approximated solution of the FEM problem is to a linearized problem and solve the equations. Since this thesis wants to study the evolution of the melt dynamics, we are interested in a prognostic solution (time dependent problems). A diagnostic (stationary) solver is used in order to achieve a good first guess for the temperature and ice velocity field. The two solver are linked to each other like illustrated in Fig. 3.4. In Comsol the solvers are implemented in the *Model tree* under the branch *Solver*.

**Diagnostic solver (Study step 1):** The purpose of the stationary solver is to find initial values for the velocity and pressure variables ( $u, v, p$  and  $u_2, v_2, p_2$ ) and the enthalpy  $E$ . In the *Stationary Solver* branch is set to solve only the above variables. These variables are solved with the linear solver *Direct*, which offers the solver types *Mumps, Paradiso or Spooles*. In this thesis the *Mumps* type is used as direct solver. This solver can be linked either with the *Fully Coupled Solver* or the *Segregated Solver*. The *Fully Coupled Solver* solves all variables at once, whereas the *Segregated Solver* solves groups of variables successively. It is called quasi Newton solver. Normally the *Segregated Solver* is not as memory intensive as the *Fully Coupled Solver*, as the later builds the Jacobian matrix for all unknowns at once, which requires computing power. The segregated solver builds one matrices for one or several unknowns. The *Stationary Solver* is linked to the *Fully Coupled Solver* as it converges faster. The solution of the stationary solver is saved in the *Solver branch*. It is later used as it serves as initial value for the time dependent solver.

**Prognostic solver (Study step 2):** The second step of the solution process is the time dependent solver. This solver technique enables us to keep track of a system's evolution over

time. It is achieved via including a time dependent solver into solver branch. All variables ( $x$ ,  $y$ ,  $u$ ,  $v$ ,  $p$ ,  $u_2$ ,  $v_2$ ,  $p_2$  and  $E$ ) are chosen to be solved here. Furthermore, the time range and the time steps are defined in the study step 2. The models run for 5 ka. This time is splitted into two sections. The first 3000 years are calculated with an intermediate time step of  $\Delta t = 1000$  a and the second from 3000 years to 5000 years with a time step of  $\Delta t = 100$  a. The solver uses an implicit time derivative principle the so called *Backwards Different Formulas* (BDF). These time step are not strictly set. Comsol offers an adaptive time stepping mode. This technique is describe by Hindmarsh et al. (2005) and changes the step size according to given tolerances. This technique is combined with a maximum value of step size, which are the time steps described above. Similar to the stationary solver the direct solver is used but is linked here to a segregated solver. This solver brings convergence to the numerical model. Four steps are added and are schematic shown in Fig. 3.4. First the enthalpy field, second the moving mesh and than the separated velocities in ice and water are solved. Each step is solved with the Newton method. The calculation of the iteration process is stop according to certain criteria. The iteration process stops either when a maximum value of iterations ( $n_{max}$ ) is reached or the relative error is smaller than the relative tolerance. The error is calculated by the weighted Euclidean norm:

$$err = \sqrt{\frac{1}{M} \sqrt{\sum_{j=1}^M \frac{1}{N} \sum_{i=1}^{N_j} \left( \frac{|E_{i,j}|}{W_{i,j}} \right)^2}}, \quad (3.6)$$

where  $M$  is the number of fields ( unknown variables solved for),  $N$  is the number Degrees of Freedom (DOFs) in field  $j$  and  $W_{i,j} = \max(|U_{i,j}|, S_j)$ , where  $S_j$  is a scale factor that the solver determines from the scaling method, in our case the damped automatic Newton method.  $U$  is the current approximation to the true solution vector, and  $E$  is the estimated error in this vector (COMSOL Inc, 2014, p. 942).

The chosen  $n_{max}$  and relative tolerances are show in Table 3.5. The whole segregates solver group has maximums iteration tolerance of 10 iterations.

Table 3.5.: Chosen maximum iteration and relative tolerances for each segregated solver step and stationary solver

Solver step	Solved variable	relative tolerance	$n_{max}$
Stationary solver	Velocities, pressure and Enthalpy ( $u$ , $v$ , $p$ , $u_2$ , $v_2$ , $p_2$ and $E$ )	$10^{-1}$	100
Segregated Solver	Velocities, pressure, Moving Mesh and Enthalpy ( $u$ , $v$ , $p$ , $u_2$ , $v_2$ , $p_2$ , $x$ , $y$ and $E$ )	1	10
Segregated step 1	Enthalpy ( $E$ )	$10^{-2}$	100
Segregated step 2	Velocities in ice ( $u$ , $v$ , $p$ )	$10^0$	100
Segregated step 3	Velocities in water ( $u$ , $v$ , $p$ )	$10^0$	100
Segregated step 4	Moving mesh ( $x$ , $y$ )	$10^{-2}$	100

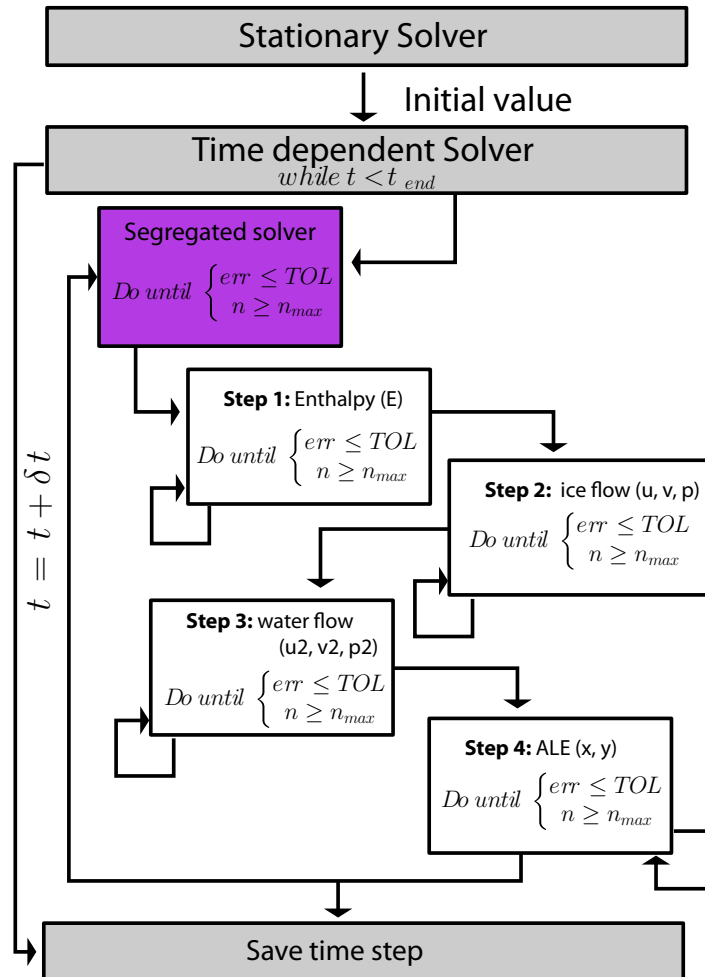


Figure 3.4.: Schematic solver diagram: The stationary solver is used to provide an initial condition for enthalpy and velocities of ice and water. The segregated solver runs in the given tolerances with the flexible time stepping mode BDF for 5 ka (modified after Beyer (2014)).

## 4. Experiments and Results

### 4.1. Experiments

In order to demonstrate the effects of subglacial water on the melt dynamics underneath ice masses and to study the creation of subglacial drainage system three main and two verification experiment are create and analysed. A list of all experiments is found in Tab. 4.1. The verification experiments are directly present in the Results section 4.2.1 and the other experiments are first present here and than the results are shown in section 4.2.

**Stagnant ice, local heat source, experiment: sub\_m1** The intention of *sub\_m1* is to investigate the responds of heat transport according to the inflow velocities and the evolution of a cavity underneath an ice sheet depending on the heat transport. Therefore, it has predefined inflow velocities at left lateral boundary of the water domain. These input velocities range over  $v_{win} = [1 \text{ mm s}^{-1}, 1 \text{ cm s}^{-1}, 10 \text{ cm s}^{-1} \text{ and } 1 \text{ m s}^{-1}]$ . The ice in this experiment has the velocity of zero  $v_i = 0$ , since the slope of the ice domain is zero ( $\alpha = 0$ ). A variation in geothermal heat flux is applied underneath the water domain at the boundary to the lithosphere. This heat flux as value of  $21 \text{ mW m}^{-2}$  at the sides and then rises to a value of  $63 \text{ mW m}^{-2}$  at the middle of the domain according to the displayed graph in Fig. 4.1. These values are chosen in order to range around commonly used value of  $42 \text{ mW m}^{-2}$  for numerical models<sup>1</sup>. The temperature of the water domain is set to pressure melting pressure temperature at the start of the simulation in order to have a water layer directly at the beginning of the calculation. Further the liquid switch is neglected as it is assumed that the water layer is constantly present.

**Stagnant ice, changing input, experiment: sub\_m2** The concept of the second experiment *sub\_m2* is that the inflow at the left lateral boundary of the water domain is dependent on liquid switch parameter and on the water thickness. This means that water is only allowed to flow if the height of the water domain exceeds the initial water thickness.

---

<sup>1</sup>The geothermal heat flux  $q_{geo}$  is set to be equal to  $42 \text{ mW m}^{-2}$ . This value is comment in ice sheet modelling. Already Greve and Hutter (1995) used it in his model. Further, he noted: „Amazingly, the numerical value 42 of the standard  $q_{geo}$  represents exactly the Answer of the Ultimate Question of Life, the Universe and Everything (Adams, 1979). Further study will be required to figure out whether this correspondence can lead to a ore profound understanding of all these things or just an accident.“ Not having found that answer the study of Ralf Greve and co has to go on.

Table 4.1.: List of all experiments

Exp. Name	Description
Verification experiments	
<i>sub_m0-p</i>	Stokes flow of ice experiment compared to results from (Pattyn et al., 2008)
<i>sub_m0-kb</i>	Moving mesh and enthalpy experiment compared to the results form (Kleiner et al., 2015)
Experiments of this study	
<i>sub_m1</i>	Stagnant ice flow with four water inflow velocities and a local heat source
<i>sub_m2</i>	Stagnant ice flow with changing water inflow velocities and a local heat source
<i>sub_m2-flat</i>	Stagnant ice flow with changing water inflow velocities and a constant heat source
<i>sub_m3</i>	Changing ice flows with four water inflow velocities, a local heat source and pre-formed water domain size.

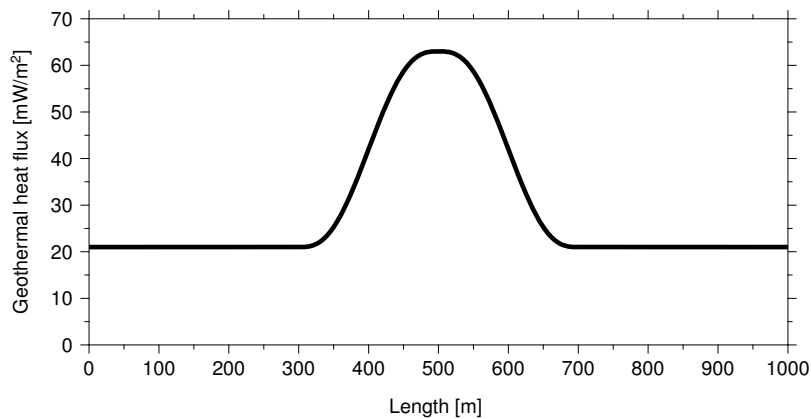


Figure 4.1.: Distribution of the geothermal heat flux applied on the boundary water/lithosphere

Further, the input velocities  $v_{win}$  have the same initial input velocities as in the experiment *sub\_m1* but depend on the height of the water domain. The relation reads as followed:

$$v_{cwin} = \begin{cases} 0 & \text{if } h_b \leq H_w \\ v_{win} \cdot h_b^{-1} \cdot H_w & \text{if } h_b > H_w \end{cases}, \quad (4.1)$$

The input velocity ranged over  $v_{win} = 1 \text{ mm s}^{-1}$ ,  $1 \text{ cm s}^{-1}$ ,  $10 \text{ cm s}^{-1}$ ,  $1 \text{ m s}^{-1}$ . This experiment has the intention to represent a potential lake drainage event. With increasing width of the drainage channel the input velocity will decrease as pressure drops. Further, the velocity of the water is non-zero in case that the water domain grew already over the original limits at the left lateral boundary.

A second setup of the experiment is created called *sub\_m2-flat*, which does not have

a variety in the geothermal heat flux. It is constant at  $42 \text{ mW m}^{-2}$  at the boundary to the water/lithosphere. All other settings are identical to the exp. *sub\_m2*. Here as well the four inflow velocities are studied in order to have corresponding model without the variation in geothermal heat flux.

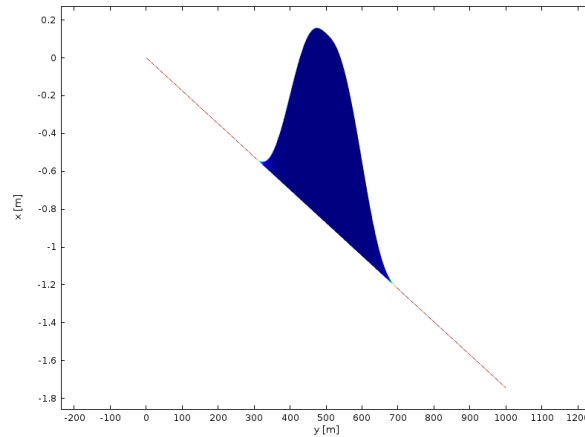


Figure 4.2.: Shape of the preset cavity with a 2 m size.

**Flowing ice, fixed water domain shape, experiment: *sub\_m3*** The third experiments *sub\_m3* couples the ice flow to the water flow. For that reason experiment *sub\_m1* is provided with a tilted slope of  $\alpha = 0.1^\circ$ . Further, it solves as well for the velocity of ice and its capability for heat transport. This third experiment is run without the evolution of the mesh, since the ALE introduced instability in the numerical model, which could not be solved until now. Two setups are created in this experiment. The height of water domain is kept constant with the original height  $h_b$  and a second setup with a cavity of a maximum height of 2 m at the center of the domain as visualized in Fig. 4.2. In order to test different ice velocities the sliding coefficient  $\beta^2$  (see Equ. 2.31) is decreased from  $\infty$  (no-slip condition) to  $50 \text{ Pa a m}^{-1}$  for a nearly free slip condition in the setup with the constant water thickness.

## 4.2. Results

The results of the three experiments are shown in the following sections and the discussion of the results follows in the next Chapter. First, the verification of the numerical model is presented. Then, the evolutions of the forming cavities are presented as well as the according melt rates. Further, the results of the flow regime in the water domain and the ice domain (depending on the experiment) will be displayed here.

### 4.2.1. Verification

Numerical models can only achieve to certain degree a claim of representing the nature (Oreskes et al., 1994). Nevertheless, the results of all numerical models have to be verified

and validated in order to reproduce and predict real world processes. The term verification means in this context that the implementation and the solutions of the underlying equations are complete and bug free. If this is the case, then the validation accords to the requirement that the numerical models represent real world processes. A verification of a numerical model can be achieved via comparing the results to an analytical solution. On the other hand the validation is done by a comparison to measured data. An intercomparison between different models is possible as well. It does not account for neither of verification and validation, which has to be kept in mind. Never the less, this verification/validation method will be done in this thesis, due to the fact that it has not yet been proven that analytical solutions exist for the Navier-Stokes equation in 3D and are smooth and further that comparing the results to data would go far beyond the scope of this study.

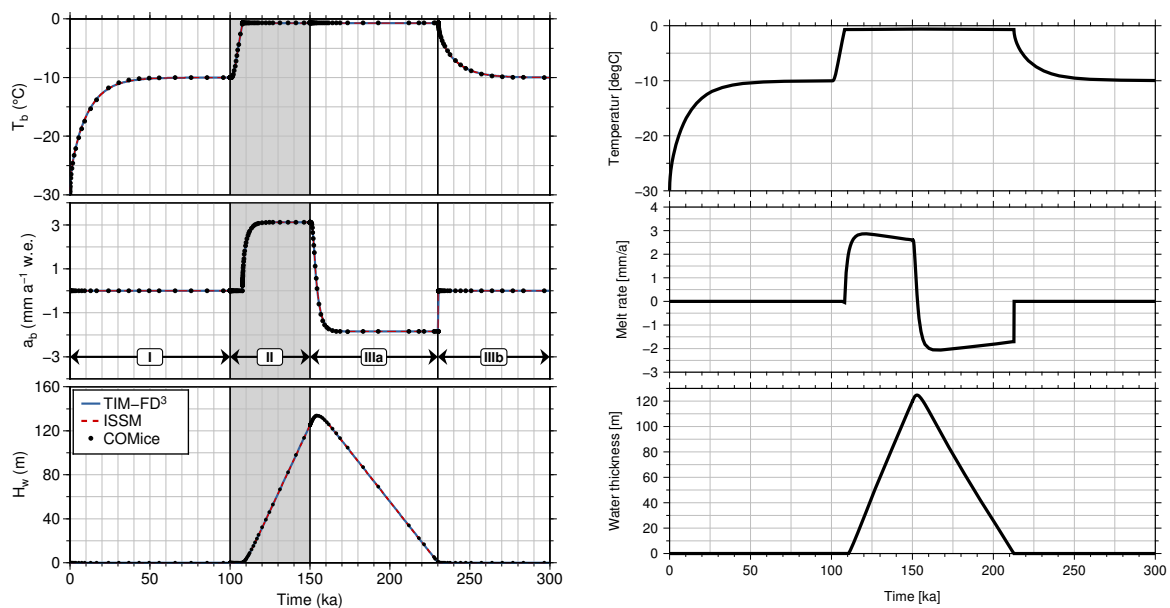
In this thesis the verification and validation is accomplished in two parts. First, the enthalpy implementation and moving mesh model is tested. For that case the verification is done with the provided benchmark experiment by Kleiner et al. (2015). The corresponding experiment is called *sub\_m0-kb*.

Second, the implementation of the Stokes flow of ice is achieved via (corresponding model *sub\_m0-p*) a comparison with the experiment D from the *ICE SHEET MODEL INTERCOMPARISON PROJECT for Benchmark experiments for numerical Higher-Order ice-sheet Models* (ISMIP-HOM) from Pattyn et al. (2008).

#### **4.2.1.1. Verification of the basal melt with the Enthalpy Benchmark by Kleiner et al. (2015)**

The benchmark experiment by Kleiner et al. (2015) Exp. A is a test of a heat transfer problem applied on an ice sheet with in particular focus on basal melt and boundary conditions. In the study three independent models are compared to an analytical solution. They find a good match between the numerical model and the analytic solution. The general set up is a 2D cut out of an ice sheet, where the boundary between ice and lithosphere a constant geothermal flux is applied of  $42 \text{ mW m}^{-2}$ . The boundary at the ice surface is kept with a Dirichlet boundary condition to a temperature, which changes over time. For the first 100 ka the temperature at the surface is set to  $-30^\circ\text{C}$  (initial phase), then rises to  $-5^\circ\text{C}$  for 50 ka (warming phase) and finally decreases to  $-30^\circ\text{C}$  again for the last 100 ka (cooling phase). The long time scales are chosen to bring the numerical model into a steady state. The changes in temperature lead to melting at the base during the warming phase. According to the melt rate a water layer develops during the warming phase and vanishes later. Here the water layer is stored at the base and does not change the original geometry. In the warming phase the basal temperature rises to the pressure melting point. After the switch from the warming to the cooling phase the water layer starts to refreeze with delay of 4 years transfer time. The temperature at the base is at pressure melting point as long as the water domain still exists. As soon as the water

layer decreases to zero the temperature drops. The melt rate experiences a jump from a negative value to zero in the moment the water domain decreases to zero. These boundary conditions are implemented into model *sub\_m0-kb* in order to represent the benchmark experiment. It has to be noted at this point that in the model *sub\_m0-kb* the water layer is not kept at the base as in the benchmark experiment but can evolve into the ice block. This difference in the setup is kept in order to see the effect of the changing geometry and test model according to the described setup. Hence, the analytical solution cannot be fully reproduced. The results of the benchmark experiments and model *sub\_m0-kb* are shown in Fig. 4.3. The results from the benchmark experiments are well represented in the verification run. The model *sub\_m0-kb* reaches the same values for maximum water thickness and maximum melt rate. Further, the model *sub\_m0-kb* reflects the temperature and melt rate switch. The general picture of benchmark experiment is well reproduced in the validation experiment *sub\_m0-kb*. In Fig. 4.4 a zoom form the temperature curve of the model *sub\_m0-kb* is shown and increase and decrease of the temperature during the warming phase is visible, which is different to the model of Kleiner et al. (2015). The difference between these two models is further explained in Discussion (see Chapter 5).



(a) Results of the Benchmark experiments by Kleiner et al. (2015) (b) Results of the corresponding numerical model *sub\_m0-kb*

Figure 4.3.: Intercomparison of the benchmark experiment by Kleiner et al. (2015) (a) and *sub\_m0-kb* (b). From up to down the following graphs are plotted: Basal Temperature, melt rate and water thickness over time.

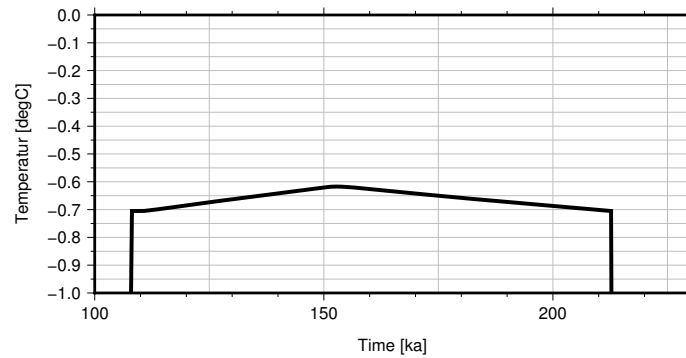


Figure 4.4.: Zoom of temperature graph during the warming phase in order to visualize the increasing temperature.

#### 4.2.1.2. Verification of the Stokes flow by the ISMIP-HOM experiment B

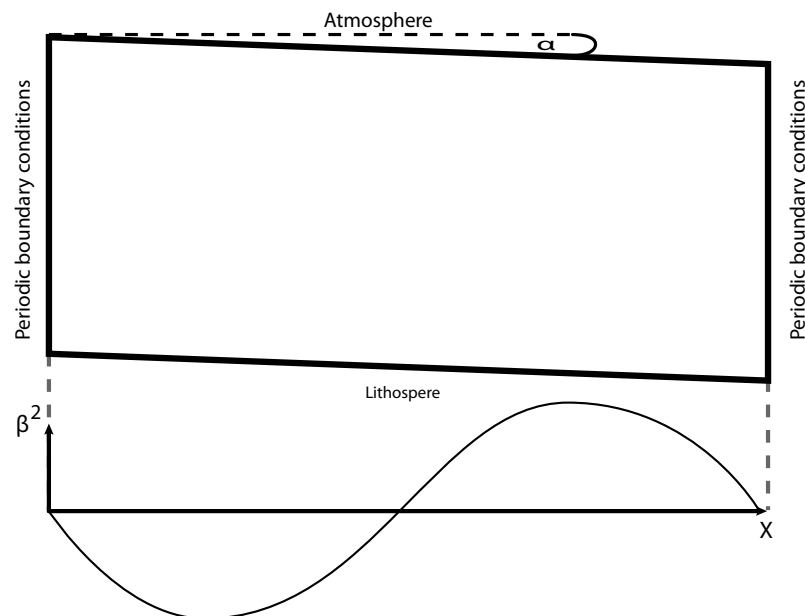


Figure 4.5.: ISMIP-HOM experiment D, a verification for the ice flow model (schematic drawing adapted from Beyer (2014))

The second verification for the model is done with a comparison to the *ICE SHEET MODEL INTERCOMPARISON PROJECT for Benchmark experiments for numerical Higher-Order ice-sheet Models* (ISMIP-HOM) by (Pattyn et al., 2008). The paper by Pattyn et al. (2008) presents six experiments (including 28 models) with different geometry setups. It includes numerical modes in 3D and 2D. Further, the paper investigates the effects of domain size, domain base geometry and friction coefficient. The results from the experiment D by Pattyn et al. (2008) is compared to the corresponding experiment *sub\_m0-p*. The experiment D is a 2D experiment and resembles an ice block, where the geometry is defined by:

$$z_b(x) = -x \cdot \tan(\alpha) \quad (4.2)$$

$$z_t(x) = z_b(x) + 1000, \quad (4.3)$$

where  $x = 0 \dots L$  with  $L = 80$  km and  $\alpha = 0.1^\circ$ . At the base a sliding law is applied from equation 2.31. The friction parameter varies over the distance and reads as followed:

$$\beta^2(x) = 1000 + 1000 \cdot \sin(\omega x), \quad (4.4)$$

where  $\omega = 2\pi/L$  is the basal friction bump frequency. At the lateral sides of the experiment periodic boundary conditions mimic a cut out from an ice sheet. The schematic drawing 4.5 show an overall model setup of the ISMIP-HOM experiment D. The model *sub\_m0-p* is adapted to the ISMIP-HOM experiment with a length of 80 km for the comparison. In Fig. 4.6 the surface velocities are plotted against the distance in a normalized scale. The velocities correspond quite well and hence, the ice flow model is verified with this intercomparison.

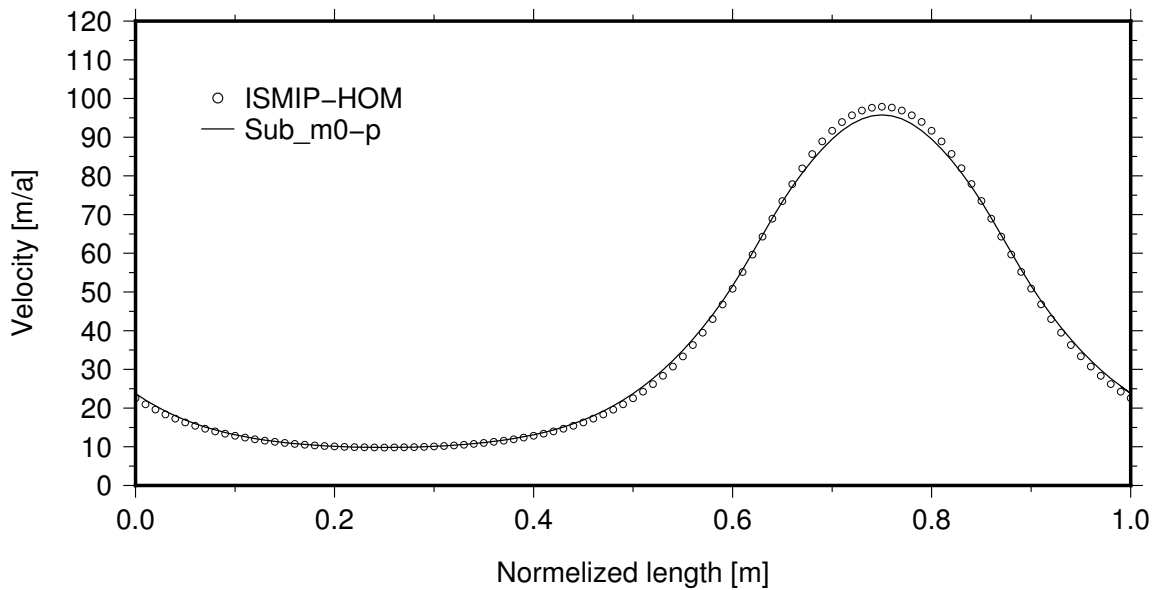
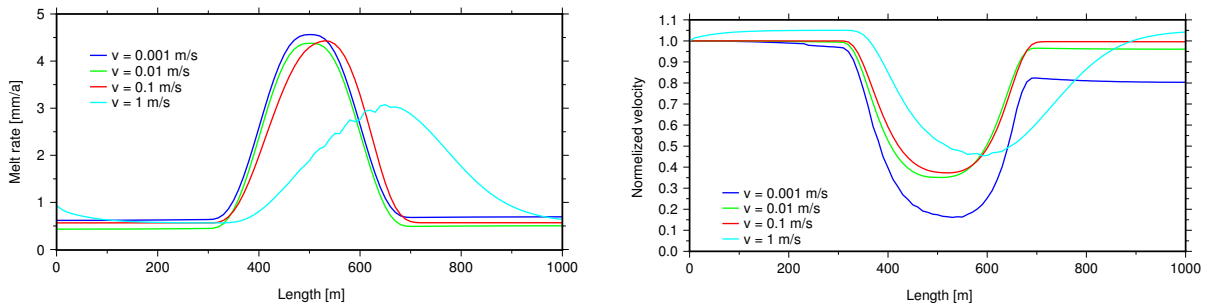


Figure 4.6.: Surface velocity profile of the ISMIP-HOM experiment D and the model *sub\_m0-p* on a normalized scale.

### 4.2.2. Exp: sub\_m1

Fig. 4.7(a) shows the melt rates along the boundary between ice and water ( $\partial\Omega_{i-w}$ ) at  $t = t_{end} = 5 ka$ . The four lines correspond in blue, green, red and cyan to the four pre-set input velocities  $v_{win} = [1 \text{ mm s}^{-1}, 1 \text{ cm s}^{-1}, 10 \text{ cm s}^{-1} \text{ and } 1 \text{ m s}^{-1}]$ , respectively. The blue curve ( $v_{win} = [1 \text{ mm s}^{-1}]$ ) is the most centred one and has the largest melt rate value, while the other curves are shifted further to the right and have significant lower values. The maximum values are present in Table 4.2. The cyan curve ( $v_{win} = 1 \text{ m s}^{-1}$ ) has the lowest maximum melt rate value. The green and red curves lie in between with their maximal melt rate value. The melt rate curve of the largest velocity (cyan curve) shows a complete different shape in contrast to the melt rate curves of the lower velocities. The three curves have a constant melt rate outside of the point heat source, while the cyan curve is first slightly decreasing between  $L = 0$  and 350 m and then rising to a maximum at  $L = 650$  m and then decreases again. Overall, the melt rates reveal a dependency of the inflow velocity. The maximum melt rate values decrease with increasing input velocity. Further, they change their shape and get shifted in flow direction.



(a) Melt rate at the boundary  $\partial\Omega_{i-w}$

(b) Water velocities at the boundary  $\partial\Omega_{i-w}$

Figure 4.7.: Melt rates and water velocities for the four input velocities  $v_{win} = [1 \text{ mm s}^{-1}, 1 \text{ cm s}^{-1}, 10 \text{ cm s}^{-1} \text{ and } 1 \text{ m s}^{-1}]$  in blue, green, red and cyan, respectively.

The water velocities at the boundary  $\partial\Omega_{i-w}$  are plotted in Fig. 4.7(b) and are normalized in respect to the prescribed inflow velocity. All curves start with a value of 1. The three lowest inflow velocities show a decreasing behaviour. The velocity drops to its minimum between  $L = 300$  and 700 m. While the green and red curve nearly reach the original inflow velocity at the right hand side, stays the blue curve at  $\approx 80\%$  of its original inflow velocity. Whereas, the cyan curves rises first and therefore increases the velocity above the input velocity. Subsequently, it drops to its minimum, which is higher compared to the other curves. Finally, it rises again to 105 % of its original input velocity. Generally the velocities decrease with increasing water thickness.

The evolution of the maximum water thickness are plotted in Fig. 4.8 and are gathered in Table 4.2. The blue curve shows the first increase in water thickness after  $t = 1.7 ka$ . While the other curves show an increase first after  $t = 4.2 ka$ . They are not

Table 4.2.: Exp. *sub\_m1*: Overview of key quantities of exp. *sub\_m1*

$v_{win}$	colour code	$\max(h_b)$ [m]	$\max(T - T_{pmp})$ [K]	$\min(v_w)$	$\max(a_b)$ [ $mm a^{-1}$ ]
$1 \text{ mm s}^{-1}$	blue	0.025	0.04	47%	4.65
$1 \text{ cm s}^{-1}$	green	0.11	0.03	37%	4.5
$10 \text{ cm s}^{-1}$	red	0.01	0.02	35%	4.35
$1 \text{ m s}^{-1}$	cyan	0.085	0.01	16%	3.22

reaching accordingly such maximum water thickness heights as for the lowest inflow velocity. Further, there is a trend visible in the maximum values linked to the input velocities. With increasing inflow velocity drops the maximum height, which is similar to the melt rates.

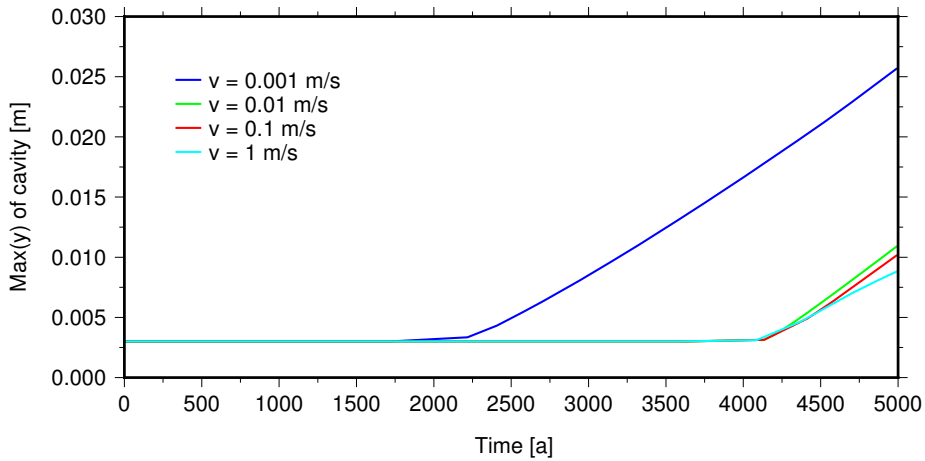


Figure 4.8.: Exp. *sub\_m1*: Water thickness over time for the four input velocities  $v_{win} = [1 \text{ mm s}^{-1}, 1 \text{ cm s}^{-1}, 10 \text{ cm s}^{-1} \text{ and } 1 \text{ m s}^{-1}]$  in blue, green, red and cyan, respectively

Fig. 4.9 displays the shape of the water domain for the four input velocities. The colour coding refers to the temperature, which is here plotted in reference to the pressure melting point  $T_{pmp}$ . The relative temperatures in the water domain vary between  $\Delta T = 0$  and  $0.006 \text{ K}$ . The temperature field changes with increasing  $v_{win}$ . It appears that the field is shifted to the right in the directions of water flow. Moreover, the maximum temperature decreases with increasing flow velocity as shown in Table 4.2.

The streamlines are also plotted in Fig. 4.9. Streamlines represent the flow vector field at one point in time. So they show the path a particle would take at that point of time. In experiment *sub\_m1* they all mimic the shape of the cavity. This means that at the sides the streamlines are nearly parallel to the bottom. In the cavity they are rising according to the shape of the cavity, whereby the lower streamlines smoother than the upper streamlines.

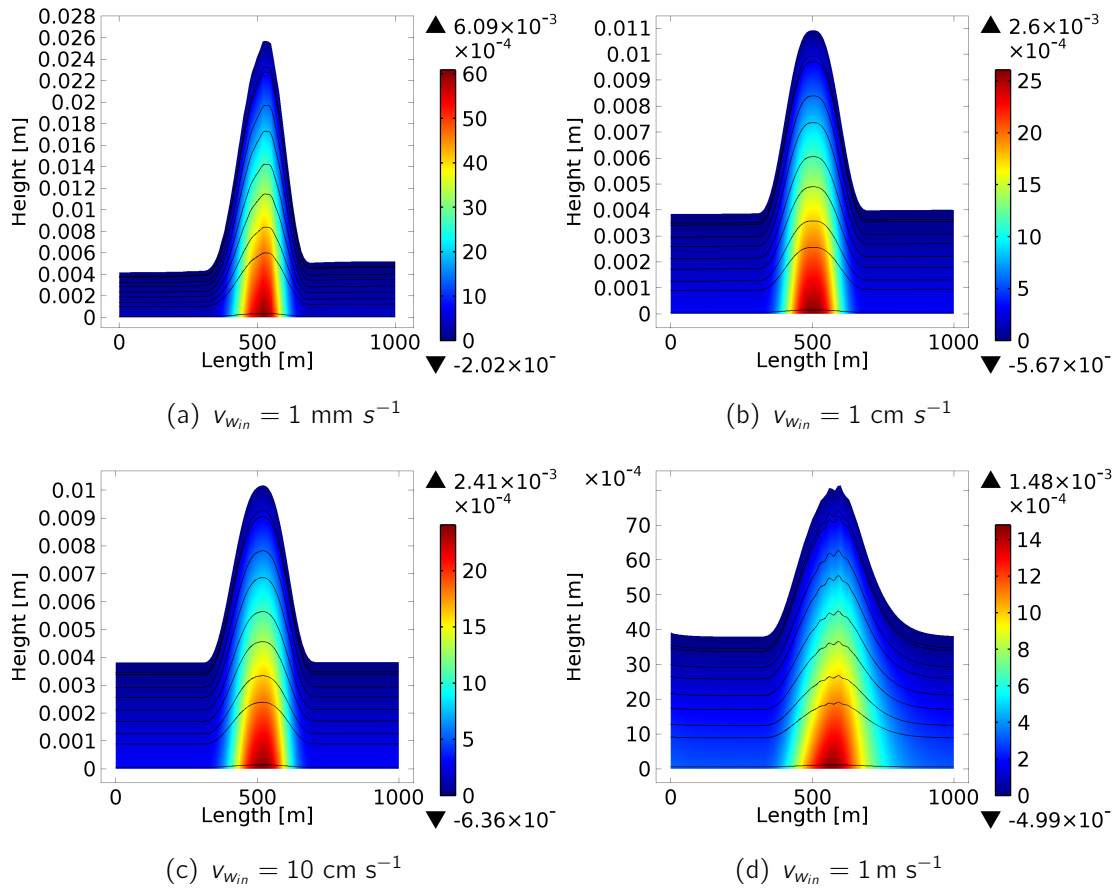


Figure 4.9.: Exp. *sub\_m1*: Water domain at  $t = t_{end}$  with the temperature field  $T - T_{pmp}$  [K] and streamlines in black for  $v_{w,in} = [1 \text{ mm s}^{-1}, 1 \text{ cm s}^{-1}, 10 \text{ cm s}^{-1} \text{ and } 1 \text{ m s}^{-1}]$

### 4.2.3. Exp: *sub\_m2*

In Fig. 4.10(a) the melt rates are shown at the end of the simulation. The blue and green curve are nearly symmetric, where by the green curve is slightly shifted to the right by  $L = 510 \text{ m}$ . The red curves show the largest melt rates (see Table 4.3) and a steeper rising and falling to the maximum than for the lower velocities. The cyan curve similar to the experiment *sub\_m1* shows no constant melt rates at the sides. In this experiment the melt rate is lower at the left side than the other velocities, which is the opposite behaviour to the first experiment. Further, the melt rate decreases before reaching its maximum at around  $L = 700 \text{ m}$ . After the maximum the melt rate drops down to a value of  $a_b = 1.3 \text{ mm a}^{-1}$ .

The velocities at the boundary  $\partial\Omega_{i-w}$  (in normalized form) show a decreased inflow velocity at the left hand side (Fig. 4.10(b)). The original inflow velocities of  $1 \text{ mm s}^{-1}$ ,  $1 \text{ cm s}^{-1}$  and  $10 \text{ cm s}^{-1}$  are reduced by 35%, while the cyan curve (largest inflow velocity) shows only a decrease of 20%. The first three velocities decrease between  $L = 300$  and  $700 \text{ m}$  to around 10% of the original value. The red curve shows a slight shift to the right again. All reach the same percentage again after the minimum than before it. The cyan curve

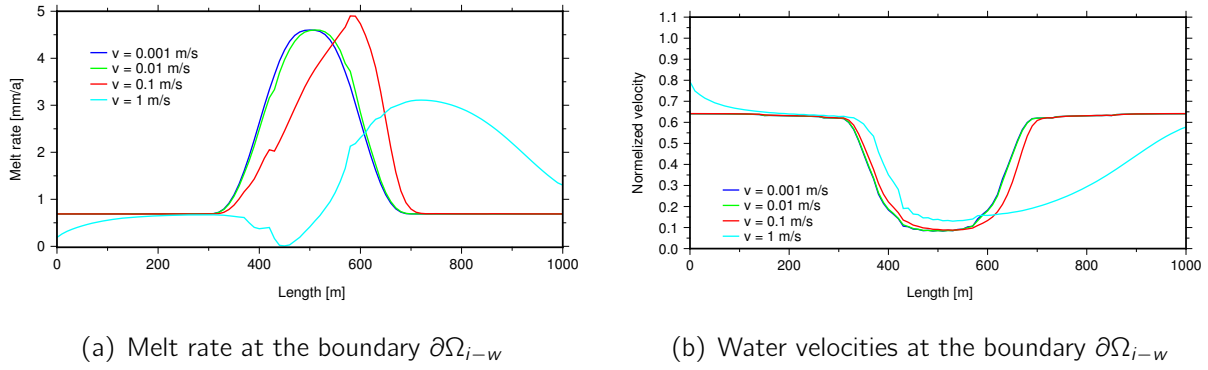


Figure 4.10.: Exp. *sub\_m2*: Melt rate and normalized water velocities at the boundary  $\partial\Omega_{i-w}$  for the four input velocities  $v_{w,in} = [1 \text{ mm s}^{-1}, 1 \text{ cm s}^{-1}, 10 \text{ cm s}^{-1}$  and  $1 \text{ m s}^{-1}]$  in blue, green, red and cyan, respectively.

Table 4.3.: Exp. *sub\_m2*: Overview of key quantities of exp. *sub\_m2*

$v_{w,in}$	color code	$\max(h_b)$ [m]	$\max(T - T_{pmp})$ [K]	$\min(v_w)$	$\max(a_b)[mm a^{-1}]$
$1 \text{ mm s}^{-1}$	blue	0.025	0.04	8%	4.6
$1 \text{ cm s}^{-1}$	green	0.11	0.03	8%	4.6
$10 \text{ cm s}^{-1}$	red	0.01	0.02	8.9%	4.9
$1 \text{ m s}^{-1}$	cyan	0.085	0.01	13%	3.1

has similar to exp. *sub\_m1* a different behaviour. The minimum in velocity is reached further to the right and the flowing increase is less steep than for the other velocities.

The maximum water thickness values in Fig. 4.11 show that until  $t = 3500$  a the max values are equal. After that time is the gradient of blue (the blue curve is hidden behind the green curve), green and red curve nearly unchanged. The red curve has a slightly lower gradient. These three curves cluster around the same final value. The cyan curves show a dramatic change in gradient behind this point. It increases far less than the other curves.

The view on the evolved water domain shapes with the plotted streamlines in Fig. 4.12 reveals that nearly the entire water domain is at pressure melting point. The shape of the cavity is for the three lowest inflow velocities nearly symmetric, while the shape of Fig. 4.12(d) shows a clear deformations. It is shifted to the right with a steep flank on the left side and gentler slope on the right side. Similar to experiment *sub\_m1* follow the streamlines the shape of the cavity, while the lower stream lines are more smooth than the upper ones.

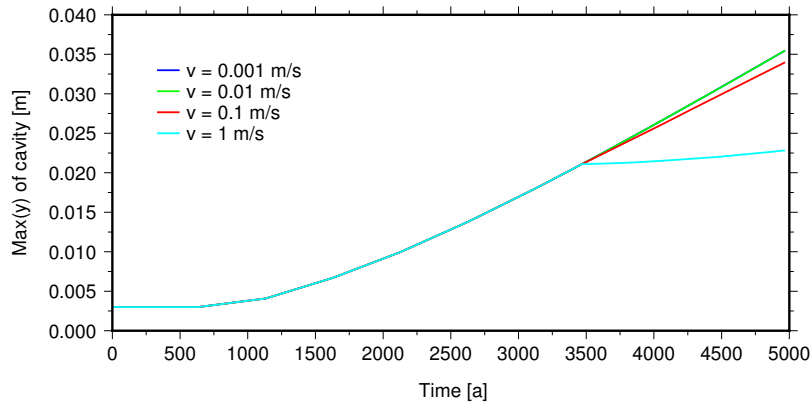


Figure 4.11.: Exp. *sub\_m2*: Water thickness over time for the four input velocities  $v_{win} = [1 \text{ mm s}^{-1}, 1 \text{ cm s}^{-1}, 10 \text{ cm s}^{-1} \text{ and } 1 \text{ m s}^{-1}]$  in blue, green, red and cyan, respectively.

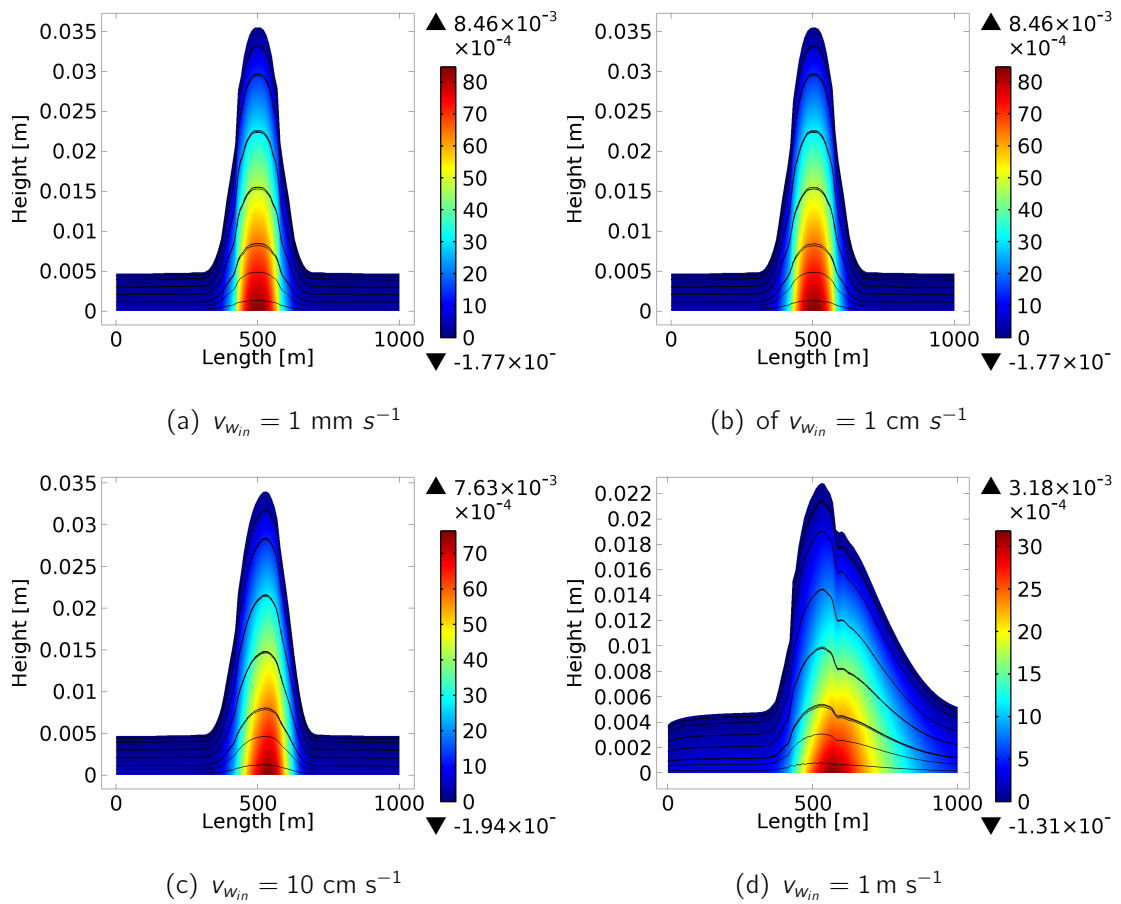


Figure 4.12.: Exp. *sub\_m2*: Water domain at  $t = t_{end}$  with the temperature field  $T - T_{pmp}$  [K] and streamlines in black for  $v_{win} = [1 \text{ mm s}^{-1}, 1 \text{ cm s}^{-1}, 10 \text{ cm s}^{-1} \text{ and } 1 \text{ m s}^{-1}]$

#### 4.2.4. Exp: sub\_m2-flat

Experiment *sub\_m2-flat* shows a different behaviour in melt rate, flow speed and cavity shape. In Fig. 4.14(a) the melt rates are plotted. Again the four colours represent the four inflow velocities. All melt rates are constant at  $a_b = 2.6 \text{ mm a}^{-1}$  except for the inflow velocity of  $1 \text{ m s}^{-1}$  which increases from left to right from  $a_b = 0 \text{ mm a}^{-1}$  to  $2.6 \text{ mm a}^{-1}$ .

Fig. 4.14(b) shows the water velocities at the boundary  $\partial\Omega_{i-w}$  and here all inflow velocities are decreased to 13% while the largest velocity shows a velocity decrease of 46% at the left hand side and then decreases further to 13% as well.

Similar to the other experiments in Fig. 4.13 the geometrical shape, the streamlines and the relative temperature  $T - T_{pmp}$  is plotted. The three lowest velocities show the same picture. The water domain reaches a height of  $H_w = 2.2 \text{ cm}$  and a linear temperature profile. The maximum temperature is at the bottom of  $\Delta T = 3.38 \cdot 10^{-4} \text{ K}$  and decreases to zero at the top. In the case of the largest inflow velocity the temperature field is shifted to the right and the water domain increases in size from the left to right. The streamlines for all four velocities follow the water domain shape.

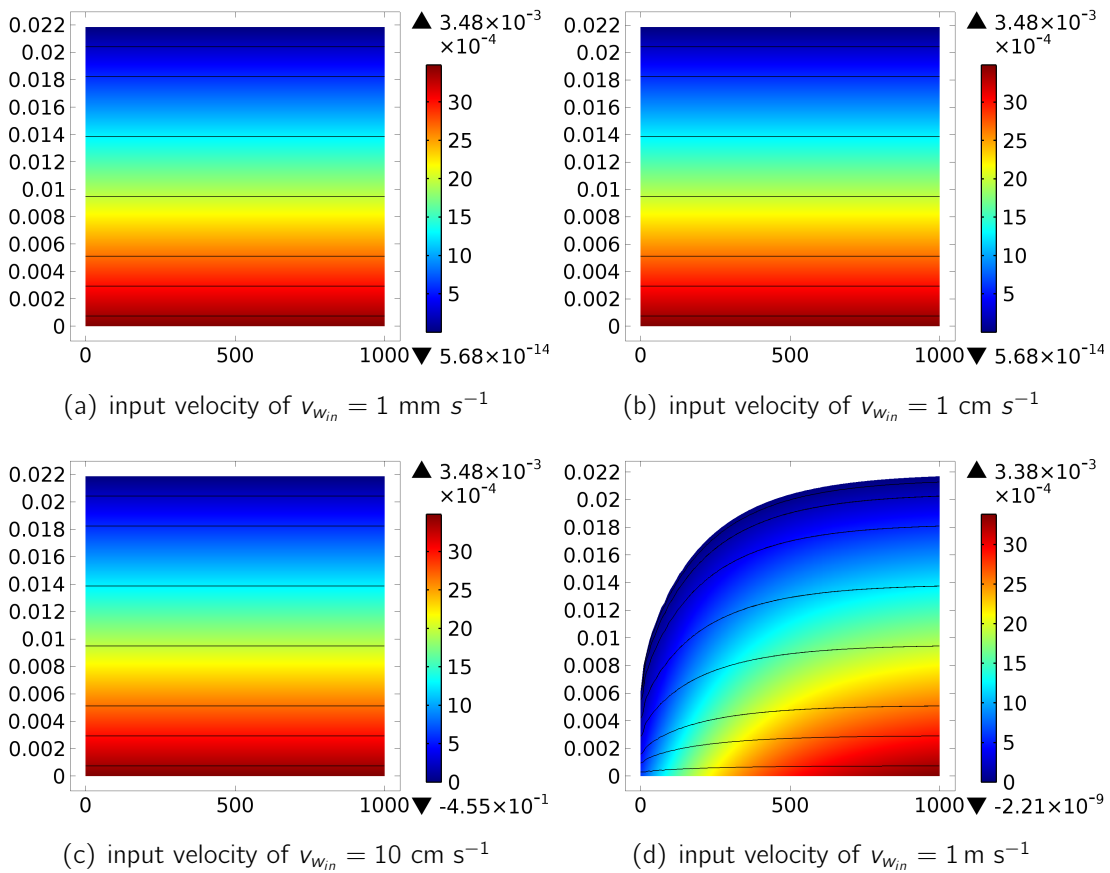


Figure 4.13.: Exp. *sub\_m2-flat*: Water domain at  $t = t_{end}$  with  $T - T_{pmp}$  [K] and streamlines in black for  $v_{win} = [1 \text{ mm s}^{-1}, 1 \text{ cm s}^{-1}, 10 \text{ cm s}^{-1} \text{ and } 1 \text{ m s}^{-1}]$

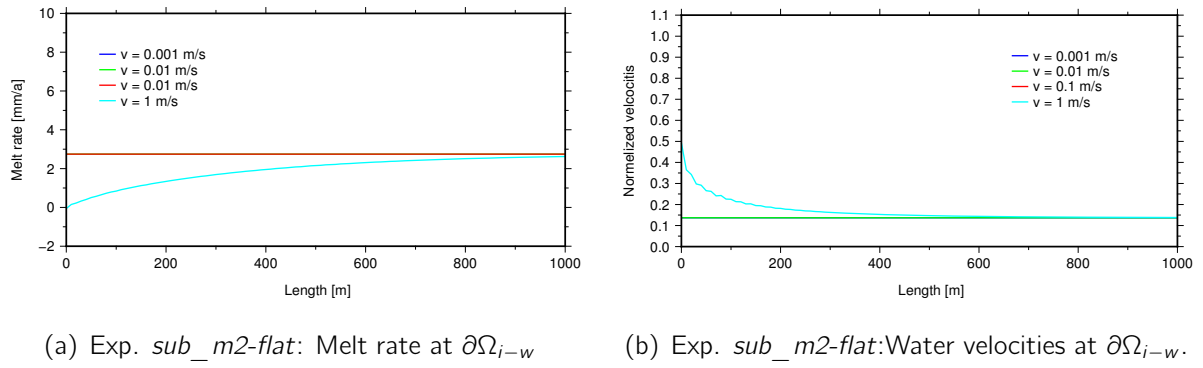


Figure 4.14.: Exp. *sub\_m2-flat*: a) Melt rate and b) water velocity at the boundary  $\partial\Omega_{i-w}$  for the four input velocities  $v_{w_{in}} = [1 \text{ mm s}^{-1}, 1 \text{ cm s}^{-1}, 10 \text{ cm s}^{-1} \text{ and } 1 \text{ m s}^{-1}]$  in blue, green, red and cyan, respectively.

#### 4.2.5. Exp: *sub\_m3*

The melt rates of the model *sub\_m3* are plotted in Fig. 4.15. The solid lines represent the setup with a straight water domain. The green and red curve is nearly centred with their maximum at  $L = 500 \text{ m}$ . The melt rates at the sides are constant and reach approximately the same values at both sides. The cyan curve is shifted to the right, its maximum is at  $L = 550 \text{ m}$ . Further, it reaches a larger melt rate at the right side than on the left side.

The dashed curves represent the melt rates for four input velocities in the setup with a preformed cavity. The green curve shows a constant value at the left side and after  $L = 320 \text{ m}$  it rises to the maximum at  $L = 628 \text{ m}$  and then drops rapidly to the pre cavity values. The other velocities show sharp rises to peak at  $L = 680 \text{ m}$  (red) and at  $L = 696 \text{ m}$  (cyan). The melt rate values are listed in Tab. 4.4.

Table 4.4.: Melt rate values of exp. *sub\_m3*

$v_{w_{in}}$	color code	$\max(a_b)[\text{mm a}^{-1}]$	at length [m]
Setup 1, straight water domain			
		$v_i \approx 2 \text{ m s}^{-1}$	$v_i \approx 300 \text{ m s}^{-1}$
$1 \text{ mm s}^{-1}$	blue	2.78	500
$1 \text{ cm s}^{-1}$	green	2.8	501
$10 \text{ cm s}^{-1}$	red	2.85	501
$1 \text{ m s}^{-1}$	cyan	3.35	535
Setup 2, cavity shaped water domain			
$1 \text{ mm s}^{-1}$	blue	2.9	555
$1 \text{ cm s}^{-1}$	green	5	628
$10 \text{ cm s}^{-1}$	red	680	
$1 \text{ m s}^{-1}$	cyan	25.6	696

In Fig. 4.16 the water velocities at the boundary  $\partial\Omega_{i-w}$  are plotted according to the four inflow velocities in normalized form. Visible is only the cyan curve, since all curves are plotted over each other. All velocities drop down to next to zero in in the range of the cavity and than rise again to the pre cavity values.

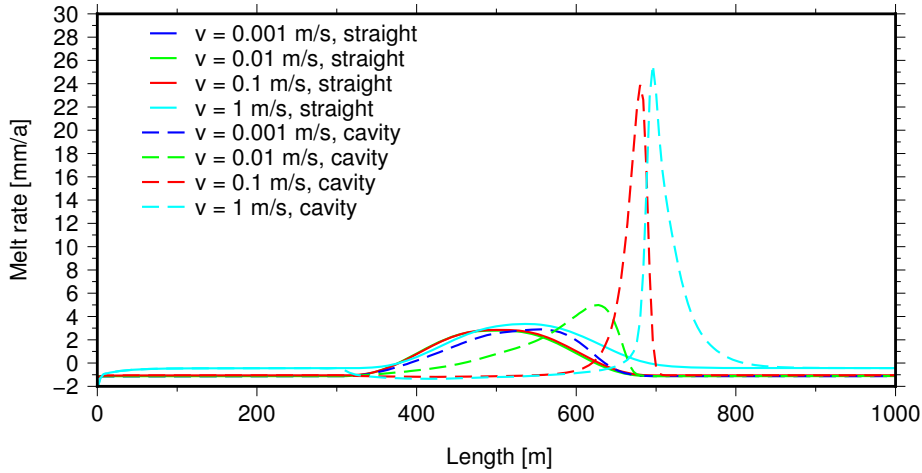


Figure 4.15.: Exp. *sub\_m3*: Melt rate of the two setups: constant Water thickness (solid) and water thickness with the cavity (dashed) for  $v_{win} = [1 \text{ mm s}^{-1}, 1 \text{ cm s}^{-1}, 10 \text{ cm s}^{-1} \text{ and } 1 \text{ m s}^{-1}]$

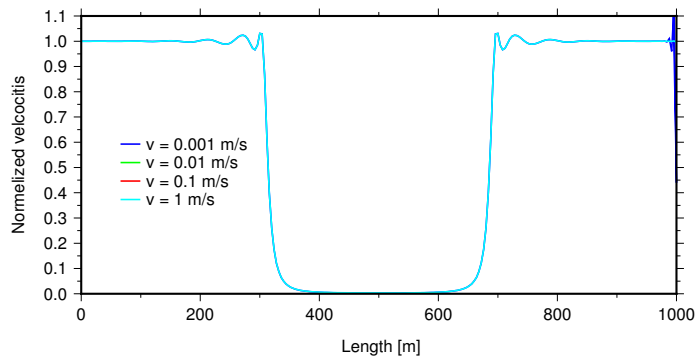


Figure 4.16.: Exp. *sub\_m3*: Water velocities at boundary  $\partial\Omega_{i-w}$  for the cavity setup with  $v_{win} = [1 \text{ mm s}^{-1}, 1 \text{ cm s}^{-1}, 10 \text{ cm s}^{-1} \text{ and } 1 \text{ m s}^{-1}]$

In Fig. 4.18 the resulting melt rates at the end of the simulation are shown for the two ice velocities  $v_i \approx 2, 300 \text{ m a}^{-1}$  (according to the friction coefficient  $\beta^2 = \infty$  or  $50 \text{ Pa a m}^{-1}$ , respectively) for the setup with the constant water thickness. The ice velocities emerge from the difference in the chose of friction parameter. There is no great divergence between the melt rates. Except the melt rate curve for the lower ice velocity and the largest water flow velocity differs in maximum position and melt rate outside of the region of increased melt rate.

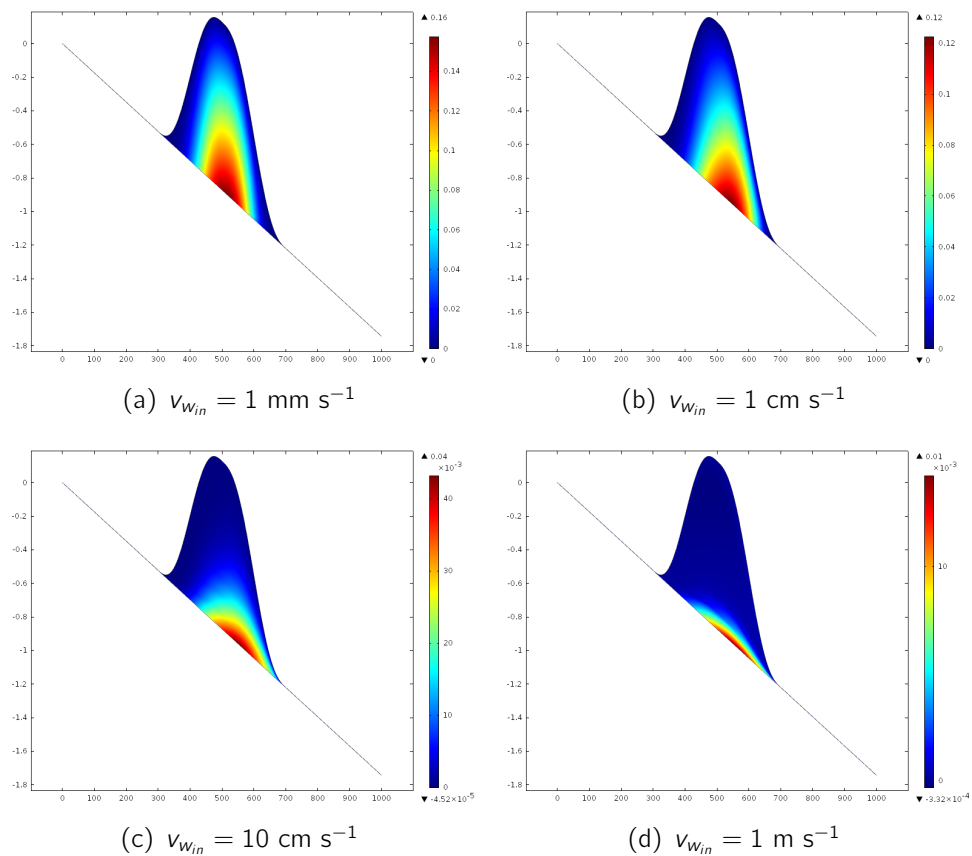


Figure 4.17.: Exp. *sub\_m3*: Water domain at  $t = t_{end}$  with the temperature field  $T - T_{pmp}$  [K] for  $v_{win} = [1 \text{ mm s}^{-1}, 1 \text{ cm s}^{-1}, 10 \text{ cm s}^{-1} \text{ and } 1 \text{ m s}^{-1}]$

The temperature field relative to the pressure melting point  $T_{pmp}$  for the setup with cavity is plotted in Fig. 4.17. With increasing inflow velocity the temperature field is further shifted to the right hand side. The highest temperature difference of  $\Delta T = 0.16 \text{ K}$  is reach in experiment with the lowest inflow velocity, while only a temperature difference of  $\Delta T = 0.01 \text{ K}$  is reached during the largest inflow velocity.

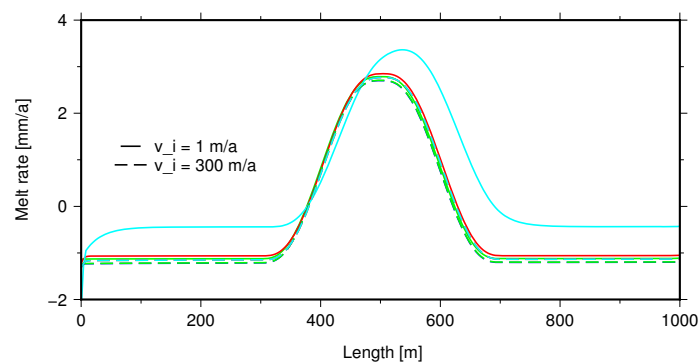


Figure 4.18.: Comparison with of exp: *sub\_m3* with a constant water thickness and different ice velocities  $v_i \approx 2, 300 \text{ m s}^{-1}$  (solid, dashed, respectively) with equal colour coding.

## 5. Discussion

This master thesis deals with different aspects of subglacial water modelling. The state of the art enthalpy formulation of for ice sheets by Aschwanden et al. (2012) is coupled with the Navier-Stokes equation in order to model ice and water flow at the same time. The Arbitrary Lagrangian Method (ALE) is used in order to evolve the water and ice domain depending on the melt rates and study the formation of subglacial water systems. Therefore, the discussion includes the topics of the verification experiment *sub\_m0-kb*, the feasibility of modelling subglacial water using Navier-Stokes flow, the results of the experiments *sub\_m1-3* and an inter comparison between the experiments.

### 5.1. Verification experiments

The verification experiment for the Stokes flow of ice with a variation of the friction parameter (*sub\_m0- $\rho$* ) is in well agreement with the benchmark experiment ISMIP-HOM D by (Pattyn et al., 2008). Hence, it is not further discussed here. The verification experiment *sub\_m0-kb*, which is compared to the benchmark experiment by (Kleiner et al., 2015), represents well the overall picture of the benchmark experiment. Nevertheless, there are some important differences, which will be discussed in the following. Both experiments have a similar setup but differ in the implementation. Hence, the two experiments are not directly comparable but they show similar behaviours. Kleiner et al. (2015) uses a external water domain in their experiments, which is evolving the water thickness separated from the ice domain. Therefore, the geothermal heat flux enters directly into the ice domain, which changes the boundary conditions according to the separately calculated water thickness to a Dirichlet condition if water is present at the base. The ice domain does not change shape and size during the simulation.

In comparison the model *sub\_m0-kb* uses a water domain, which evolves into the ice domain. The geothermal heat flux enters first into the water and than into the ice domain.

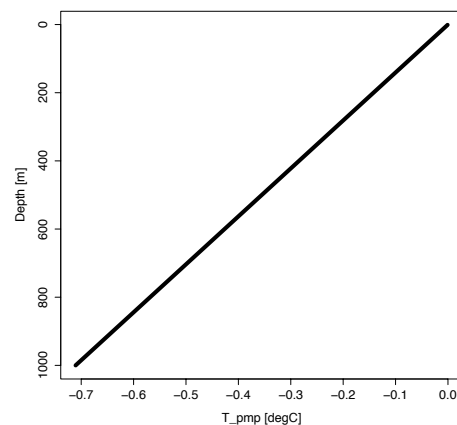


Figure 5.1.: Pressure melting point temperature  $T_{pmp}$  dependent on the depth in an ice sheet with constant density ( $\rho_{ice} = 910 \text{ kg m}^{-3}$ )

This changes the thermal conductivity values from ice to water, which leads to different gradients in the domains. Moreover, the boundary between ice and water moves in the domain taking effect on the heat transport. This affects further the Dirichlet condition, because the increase of water domain includes a corresponding decrease of the ice domain thickness, resulting in a pressure change at the boundary  $\partial\Omega_{i-w}$ . The pressure melting point changes according to the pressure change. It is visible in Fig. 4.4. An increase in water thickness results therefore in increase in  $T_{pmp}$  like visualized in Fig. 5.1. The change in pressure melting point temperature has the effect that the fluxes at the boundary  $\partial\Omega_{i-w}$  change over time, which influence the melt rate. It is clearly visible in Fig. 4.3(a) in the melt rate window. The decrease and increase in melt rate after the maximum and minimum respectively, results from the change in heat fluxes.

The moving boundary also explains the difference in timing. The cold wave from the cooling phase can reach the water domain earlier since it has to travel only 880 m (in the *sub\_m0-kp* model) instead of 1000 m (in the Kleiner et al. (2015) benchmark experiment). This leads to an earlier decrease to negative melt rates and an earlier vanishing of the water domain.

The comparison shows that on the one hand the model *sub\_m0-kp* can be verified with the benchmark experiment. On the other hand it clarifies that a changing geometry has effects on melt dynamics, which cannot be neglected. Nevertheless, these differences are intendant, in order to study their effects. Moreover, it illustrates that the presents of water changes the melt dynamics significantly.

## 5.2. Feasibility of modelling subglacial water using Navier-Stokes flow

One major task of this thesis is to investigate the possible usage of the Navier-Stokes flow for both water and ice combined as a thermo-mechanical problem and solved in the same system. This coupling shall give insight to melt dynamics underneath ice masses and their possible implications on ice dynamics. Here, a conceptual numerical model demonstrates the possible coupling of these physical processes.

In a general this problem is a so called a Stefan's problem (Stefan, 1888), which describes the phase change between solid and liquid, linked to Navier-Stokes flow. The possible coupling is proven with the experiments described below and their verification is proven by the experiments *sub\_m0-p* and *sub\_m0-kb*. Nevertheless, they need an overall discussion in order to place them in a broader context and present problems, which have to be overcome.

**Timestep:** As described in the Implementation Chapter 3.1 the timestep is not fixed to a static value. Comsol has the ability of an adaptive timestepping method, which depends on an calculated error. This allows calculating with larger timesteps in cases where the numerical model approaches stationary states. In cases where great changes occur in the numerical model, the timestepping algorithm switches to small time steps. During the calculation of the experiments timesteps are reached ranging from hundreds of seconds to hundred years. The timestep changes when the water domain starts to flow. It brings a new switch into the model and the heat transfer has to adjust to this situation. Without the adaptive time stepping algorithm a simulation of this process would be computational costly, since otherwise the lowest value for the timestep would need to be overall applied as timestep. This would increase the computation time by a magnitude of  $10^9$ .

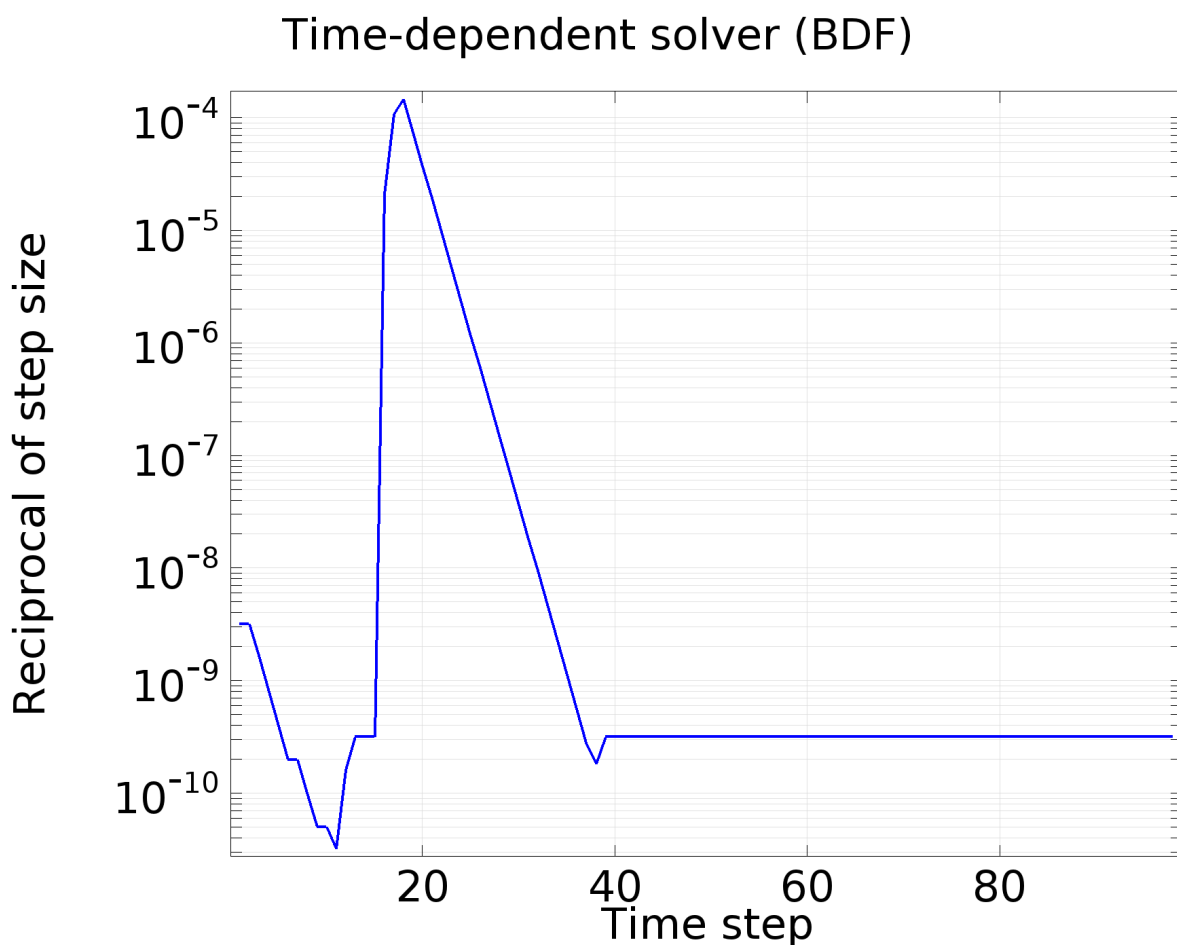


Figure 5.2.: Convergence graph of experiment *sub\_m2*, which is representative for all experiments. Plotted is the reciprocal of the timestep size over the integration number. The reciprocal of the timestep is used since it is convenient in numerical model that the convergence curve decreases.

**Smoothing of ALE:** The moving mesh is controlled by the melt rate and a smoothing parameter. This smoothing parameter decreases the input melt rate to lower values. Hence

the moving mesh does not deform in the same magnitude than prescribed by the melt rate. Nevertheless the input melt rate ratio is kept the same and the domains will change according to the melt rate ratio but not in the same order of magnitude. This is necessary to achieve numerical stabilization in the experiments, as changes in the water domain are crucial for the flow pattern. For example, a timestep of ten years with melt rate of 3 mm a<sup>-1</sup> would lead to an increase of 30 mm of the water domain, which is a tenth of initial water domain thickness. Such great changes have impacts on the flow regime, which the numerical model cannot cope with at this point of time. Hence a smoothing factor has to be introduced. Several tests showed that a value of 10<sup>-4</sup> gives the best results according to lowest smoothing value and numerical stabilisation. Therefore, the experiments experience lower deformation but as shown below already this scale of deformation leads to results of different flow regimes and hence changes in melt dynamics. Therefore, the experiments have to be treated with care but are nevertheless still significant enough for interpretation.

Another point regarding the ALE is the not yet solved coupling of the ALE to the ice flow and water flow at the same time. Experiment *sub\_m3* is a first step into that region but experienced numerical instability while coupling the three of them. This is the reason why *sub\_m3* is presented without the evolution of the mesh. Possible reasons for that is the switch in the boundary condition from a no-slip state to slip boundary condition. Moreover, the change of the ice domain shape which leads to changes in the flow of ice. These problems should be conquerable in future models. Possible approaches would be a limiting the timestep to fractions of a year or increase the amount of grid cells, which would lead to finer resolution and smoother transitions. Due to the great effort in computational time this could not be tested, yet.

### 5.3. Experiments *sub\_m1-3*

In the following the results from the three experiments will be discussed. They are the result of feasibility test modelling ice flow, water flow and melt dynamics at the same time. Each experiment is first discussed separately and finally an inter comparison is drawn in Section 5.4.

#### 5.3.1. Experiment *sub\_m1*

The experiment *sub\_m1* shows a first picture how melt dynamics could evolve underneath an ice sheet. The general setup is that a smoothed point source underneath an ice sheet creates a water layer. The water flow in the layer is controlled via different inflow velocities at the left hand lateral side of the model's water domain. Already the melt rates at the end of the simulation, shown in Fig. 4.7(a), give a clue about the different melt dynamics.

It is obvious that there is a clear trend in the peak values of the melt rates. With increasing flow velocity the melt rate peaks moves further to the right. Moreover, there

is a shape change of the melt rate curve for the largest velocity. These melt rates are a result of a combination of two affects. The first one is the water flow velocity depending on the water domain geometry. The second influence is the shape of the water domain, which is a result of the melt rates.

1. The water flow velocity has a trend as well. In Fig. 4.7(b) the normalized velocities are plotted and the drop in flow velocities occurs always in the region of the evolved cavity of the model. The drop in velocity is a consequence of the continuity equation's fulfilment. Water is an incompressible fluid, hence there cannot be any sources or sinks. This principle applied on a flow through a tube with changing diameter results in the following relation (Sigloch, 2008, p. 69) and is called the Bernouli effect:

$$v_1 \cdot A_1 = v_2 \cdot A_2, \quad (5.1)$$

where  $A_{1,2}$  are the two diameter and  $v_{1,2}$  the two velocities. A difference in diameter e.g.  $A_1 > A_2$  results in a difference in the velocity  $v_1 < v_2$ . This relationship implies as well on the forming cavity. The ration between the two diameters  $A_1/A_2$  ( $h_b/H_w$ ) for lowest inflow velocity in exp. *sub\_m1* is equal to  $\approx 12\%$ . As shown in Fig. 4.7(b) the ratio between the resulting water flow velocity and input flow velocities ( $v_w/v_{w_{in}}$ ) reaches approximately the same value in the cavity. Hence, the water domain shape triggers the change of the water flow velocity.

2. The heat transfer in all the experiments is coupled to the water dynamics. Hence, the heat advection strongly is influenced by the different flow dynamics (see Fig. 4.9). With increasing input flow velocity the temperature field is shifting further to the right, which results in a change in the heat flux distribution. Since the melt rate is calculated by the difference in heat fluxes, it is therefore changed accordingly the water flow dynamcis. The melt rates generate a new cavity shape.

Therefore the three components, melt rate, water domain shape and flow velocity, are in cyclic dependency. The connection is schematically illustrated in Fig. 5.3. As long as the geothermal heat flux is high enough to rule out refreezing at the base, which is the case in this experiment, there will be a positive feedback between melt rate, geometrical shape change and resulting flow velocity. For example, if the melt rates differ along a boundary, due to e.g. a change in geothermal heat flux, there will be an asymmetry in geometry of the water domain. The difference in water layer thickness results in lower velocities and in these regions the heat is transported more efficiently. This leads again to more melting and the process is therefore self enhancing.

The cavity formation at low velocities ( $1 - 10 \text{ mm s}^{-1}$ ) is lesser influenced than at larger velocities as a nearly symmetric cavity develops (see Fig. 4.9(a), 4.9(b)). Moreover, the setup with the lowest input velocities develops the largest cavity and has even an earlier

start of cavity evolution. This implies that diffusive heat transport overcomes the advective heat transport for the three lower inflow water velocities.

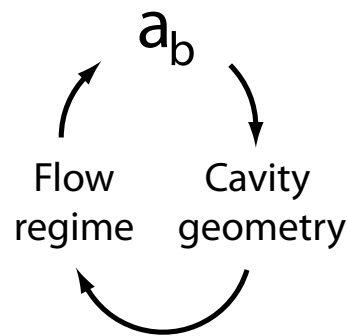


Figure 5.3.: Schematic illustration of positive feedback

In Fig. 4.9 the streamlines are also displayed. They give the general picture that the streamlines follow the shape of the cavity. These streamlines are nearly parallel to each other. Hence, the whole flow regime is laminar. This flow regime results from the low change in cavity size and the free slip boundary condition. A no slip condition at the top and bottom boundary of the water domain could lead to enhancement toward a turbulent flow regime. Such a boundary condition would simulate enhance friction at the base and leads to a turbulent boundary layer (Schlichting and Gersten, 1997). The turbulent boundary layer affects the heat transfer by diminishing the heat transport. Hence a turbulent water layer would decrease the melt rates. Subglacial channels underneath glaciers have a huge roughness and their effect on water flow has already been proven by Gulley et al. (2009). Since this master thesis deals more with the coupling of the ice and water flow including melt dynamics, it is an effect, which has to be included in future experiments.

Overall, the results of exp. *sub\_m1* show that there is a link between cavity shape, inflow water velocity and melt rate, which coupled in a positive feedback as long the geothermal heat flux permits no refreezing. Further, it is visible that the flow is laminar and no turbulence occurs.

### 5.3.2. Experiment *sub\_m2*

The experiment *sub\_m2* intentioned to model melt dynamics linked to changes in inflow velocities. This reflects drainage of a subglacial lake. The inflow velocity  $v_{win}$  is decreased with the increasing water thickness. The inflow is set to zero as long as the water thickness is quantified as not *liquid* at the left lateral side. The variation in geothermal heat flux leads to a pre-formation of the water domain during a phase of no water flow. First a

cavity develops and then the region outside the increased geothermal heat flux starts to move upward. The cavity starts to deform with initialisation of the input velocity.

Regarding that fact explains the behaviour of the maximum water thickness values in Fig. 4.11. All setups start with a zero inflow velocity, which enables the water domain to rise first in the region of increased geothermal heat flux. After 3.49 ka the water flow starts to interfere into the melt rate. At that point the curves start to diverge. The low inflow velocities ( $1 \text{ mm s}^{-1}$  -  $0.1 \text{ m s}^{-1}$ ) are stronger effected as the inflow velocity of  $1 \text{ m s}^{-1}$ . This is also underlined by the cavity shape in Fig. 4.12. The three lower velocities have a nearly symmetrical shape in contrast to the largest velocity. In the experiment *sub\_m2* the flow velocities above  $v_{w_{ing}} = 10 \text{ cm s}^{-1}$  take the strongest influence on the melt rate and hence the geometry. For the exp. *sub\_m2* it has to be kept in mind that the pre-set inflow velocities are scaled by the inflow condition according to the Bernoulli effect. As shown in Fig. 4.10(b) the water inflow is already decreased to values between 60% and 80% at the left side (boundary with prescribed inflow velocity). At the end of the simulation the water thickness at the inflow boundary increased to a value of  $H_w = 0.0045 \text{ m}$  for three lowest velocities and to  $H_w = 0.0038 \text{ m}$  for the greatest inflow velocity, which leads to a decrease of 36% and 21% respectively. Similar to *sub\_m1* the velocities decrease in the range of the developed cavity due to the Bernoulli effect. The nearly symmetric cavities show a corresponding behaviour in the flow velocities. The largest input velocity shows a different behaviour in comparison to the other velocities. Since this setup reaches the lowest cavity size it is an obligation that the decrease is not as strong as the others.

The melt rate, as already described above, is influenced by the thermal regime and therefore a result of the flow regime. The melt rates for the two lowest inflow velocities are nearly identical. The two larger velocities create a more irregular melt rate shape and are discussed more in detail here.

In Fig. 4.12(d) the temperature distribution affirms the melt rate for the setup of  $v_{w_{in}} = 1 \text{ m s}^{-1}$ . The heat is shifted to the right, which increases the melt rate at the right side of the cavity. The double ridge (see Fig. 5.4) on the right side of the cavity is a reaction to two melt rate regimes (compare Fig. 5.4). The first cavity forms during the time while  $v_{w_{in}} = 0 \text{ m s}^{-1}$  and the second during  $v_{w_{in}} > 0 \text{ m s}^{-1}$ . Striking in the melt rate curve is as well the minimum before the rise to the maximum. Such a behaviour is unique in comparison to the other curves. The decline comes from the changing temperature field. As more heat is transported with the water flow and is "missing" on the left hand side of the cavity. The cavity moves therefore in the direction of water flow over time. A similar trend, which is not as strong, is noticeable for the  $v_{w_{in}} = 10 \text{ cm s}^{-1}$ . The melt rate curve indicates already a future change of the nearly symmetric cavity shape. The temperature regime deviates from the initial position and leads to an enhanced melt rate. The step at the right hand side of the melt rate curve thus reflects the decreased heat flux on that

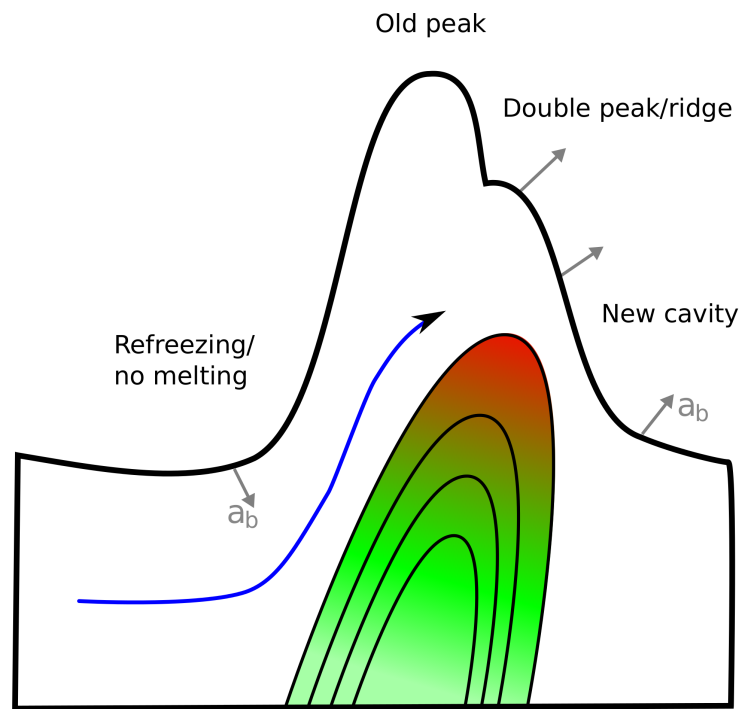


Figure 5.4.: Schematic cavity transformation at critical velocities.

side.

The second part of the experiment, (*sub\_m2-flat*), uses a constant geothermal heat flux at the boundary water lithosphere of  $42 \text{ mW m}^{-2}$ . The intention of this experiment is to investigate if a thin water layer can evolve into a different drainage system.

The value of the geothermal heat flux does not match the value of the geothermal heat flux at the side of the above experiments. They use a heat flux of  $21 \text{ mW m}^{-2}$  at the sides. The difference arises from the point that the later described effect is clearer visible with a geothermal heat flux of  $42 \text{ mW m}^{-2}$ . For completeness the geothermal heat flux of  $21 \text{ mW m}^{-2}$  was tested with this setup as well. The results mimic the behaviour of the described results and are in accordance with the water thickness reached by the first setup *sub\_m2*, but are not as strong. The experiment *sub\_m2-flat* shows that water domain is in a positive feedback to the melt rate and flow velocities. The inflow velocities between  $v_{w,in}=0.001$  and  $0.1 \text{ m s}^{-1}$  show that at this order inflow velocity the heat is evenly distributed in the water domain. It needs an initial inflow velocity of  $1 \text{ m s}^{-1}$  in order to start changing the water domain or perhaps longer simulation runs. Here the fast water velocity transports the heat way from the left hand side of the domain, which results in a lower melt rate at the left side of the boundary  $\partial\Omega_{i-w}$ . The water domain starts to deform asymmetrically and results in a change of the flow regime. The establishing water velocities are larger on the left hand side and lower on the right hand side. Since the lower velocities favour the heat transport the system is in constant change. At the beginning of

the simulation the advective heat transport overcomes the diffusive part in this scenario and the cavity start to deform asymmetrically. Hence, the Bernouli effect changes the flow velocity as shown in Fig. 4.14(b). The melt rates verify that picture. Moreover, this scenario demonstrates the possibility of a subglacial water system to switch form a sheet flow to a channelized flow type, when a critical water velocity is reached. This fact will be discussed further down.

Overall, the experiment *sub\_m2* is in well accordance to experiment *sub\_m1*. Both follow the described relationship from Fig. 5.3. A clear change in the melt rate behaviour at velocities above  $v_{w,in} = 10 \text{ cm s}^{-1}$  indicates a critical velocity value, which is also proven by the experiment *sub\_m2-flat*. At those flow speeds a significant change in cavity geometry occurs after 5 ka of simulation, which triggers further change. Hence the lower velocities can be quantified as less dynamic systems. Here melt rate and flow velocities indicate a less dynamic system. This is also underlined by the experiment *sub\_m2-flat*. A critical velocity of above  $v_{w,in} = 10 \text{ cm}^{-1}$  are necessary to destabilize the subglacial water system. The experiment proves that a switch form a initial sheet flow can switch to a channelized system underneath an ice sheet by an increase in flow velocities above the named critical threshold velocity.

### 5.3.3. Experiment *sub\_m3*

The experiment *sub\_m3* has the intention to study the effects of coupling water and ice flow. Similar to the other experiments the same inflow velocities are chosen. The experiment setup did not allow coupling the ALE moving mesh transformation in model due to instability reasons. Hence, two scenarios reflect two stages in the melt dynamics. The first experiment just a straight water domain with a constant thickness of 3 mm. In the second setup the water domain increases to a cavity with a 2 m diameter according to the shape of the geothermal heat flux function. Moreover, there is a third setup, which has the aim to study the effect of enhanced ice flow on the melt dynamics. The above setups are calculated with a no-slip boundary condition at  $\partial\Omega_{i-w}$ , which leads to ice velocities of  $1.9 \text{ m a}^{-1}$  at the ice surface. In a comparison run the friction coefficient is decreased to  $\beta^2 = 50 \text{ Pa a m}^{-1}$  for the setup with the constant water thickness, which results in surface velocities of  $v_i \approx 300 \text{ m a}^{-1}$ . The setups give insight to the effects of ice and water dynamics on melt dynamics. First the effect of the ice velocities will be discussed followed by the two water domain shape setups.

The melt rates do not differ much between the two ice flow rates as shown in Fig. 4.18. The melt rates increase in the areas of enhanced geothermal heat flux. Notable is the fact that the melt rate is negative in the regions outside the increased geothermal heating.

Since the geothermal heating is set to zero at the sides of the domain, it is not surprising. The water layer would close itself around the region of increase geothermal heating. This is prevented by the experiment conditions as the boundary between water and ice cannot move and is kept at pressure melting point. Nevertheless, the enhanced geothermal heat flux is necessary to sustain a water layer with these dimensions. Under these condition the water layer would vanish in some years, which has already been described by Kleiner et al. (2015).

The comparison reveals that the dominate part on the melt dynamics is the water part. The increase in ice velocity show no significant change in the melt dynamics even than the ice velocity increases by a magnitude of 2. The water flow velocities are in orders of magnitudes higher than the ice velocity. Hence, the heat transfer is not significantly affected by the ice flow.

In the following the differences between the two setups with the lower ice velocity will be discussed. The setup with constant water thickness shows that the increased melt rate is in the nearer regions of the increase geothermal heating. Again the largest flow velocity shows the most significant shift of the melt rate curve in downstream direction.

The second setup with the pre-set cavity on the other hand shows a great diversity in melt rate behaviour. The flow velocities in the range of the cavity drop down to nearly zero % of the initial inflow velocity as shown in Fig. 4.16. Therefore, larger melt rates can be reached at the sides of the cavity since the flow velocity is even slower than the slowest velocity of the first setup. The fast flowing water transports the heat to the right side of cavity and produces largest melt rates at the right side of the cavity. The two slowest velocities show the lowest melt rates. Further, they are barely moving downstream in comparison to the other inflow velocities. In Fig. 4.17 shows the relative temperature regimes. For the low velocities the whole cavity is nearly filled with increased temperatures, which explains that the melt rates are nearly symmetrical in the cavity. With increasing flow velocity the temperature field gets shifted to the right and does not leak into the cavity any more. The heat flux is thus directed further to the side of the cavity and to the point, where the cavity is approaching its initial thickness  $h_b$ . Since most of the heat is focused on this spot the melt rates increase dramatically. Moreover, the melt rate approaches a limit, since there is barely a difference between largest melt rate values for the two largest inflow velocities. It implies that the cavity would start to move downstream.

Overall the two setups and the comparison run show that ice dynamics has a negligible influence on melt dynamics as soon as water is flowing. Further, the experiment shows that if the inflow velocities in already build up cavity increases, it leads to a refreezing of the cavity (at the upstream end of the cavity) and hence to a shifting of the cavity down stream, which is corresponds to the other experiments. A critical flow velocity is essential

for these processes since the experiments conclude that at low velocities the system appears to be less dynamic.

### 5.4. Intercomparison *sub\_m1-3*

The three experiments show a homogeneous picture of the evolution of melt dynamics in subglacial systems. An overall conclusion is that a subglacial water layer can form in regions of increased geothermal heating. Once this water flows above a critical velocity a symmetrical cavity starts to change its shape as illustrated in Fig. 5.4. In low flow regimes the advective part has significantly lesser influence than the diffusive part. This relation changes in flow regimes above velocities in the order  $\text{cm s}^{-1}$ . The influence from the ice dynamics on the heat transfer is negligible small.

All experiments show nearly no turbulent flow behaviour. This is a result on the one hand of the chosen free slip boundary condition at the top and bottom side of the water domain. The no friction boundary condition permits a laminar flow, which is proven by the streamlines. Further, the change of domain shape in vertical direction in the experiments *sub\_m1* and 2 are relatively small to the extend of the domain in horizontal direction. As described above this results form the introduced smoothing parameter for the ALE algorithm. The smoothing is necessary in order to maintain stability of the numerical model. On the other hand this restricts the formation of bigger cavities, with turbulent water fluxes. Therefore, experiment *sub\_m3* is set up with an increased cavity size. No turbulent flow establishes in this experiment, which is likely a result of the still broad extend in x direction of the cavity, since magnitude of the cavity thickness is small compared to its width. Nevertheless, the experiments show already at these dimensions an effect from the flow velocity on the melt rate. The changing water thickness results in different flow patterns, which lead to change in the melt dynamics. This is a self developing process.

Overall the experiments give insights into melt dynamics underneath ice mass. It is an important step in understanding processes, which are far from being easily surveyed by field campaigns. The experiments show that large water velocities underneath an ice sheet or differences in flow regime are necessary in order to change the melt dynamics significantly. Their implications are discussed in the next Section.

### 5.5. Implications

In this section the general implications are discussed. The topics of the steady state possibility of subglacial water, cavity location related to geothermal heat distribution and potential reverse implication on the heat flux and flow velocity will be further analysed.

All experiments are run for 5 ka, which is a long time period for water flow dynamics but in ice dynamics modelling a moderate to short time. The presented results are not at a steady state picture due to the fact that a steady state is properly not reachable. Due to the positive feedback affect the system is in constant change. The 5 ka snap shot is presented in order to give an impression at one point in time at which all models evolved a water layer and showed changes in the melt rate dynamics. For instance an ice sheet might seem to be in balance regarding ice dynamics but the results of this thesis imply that a subglacial drainage system is not in balance due to the positive feedback. Further, in the case of an increasing water domain the possibility rises to switch from a laminar flow regime to a turbulent one (Kundu et al., 2014). Such a change would lead to a better mixing of the water layer and hence to an increase of the heat transfer. Or on the other hand a turbulent boundary layer could develop at the bottom with an overlaying laminar flow regime. In this turbulent boundary layer heat would be kept and transported away. Hence a second effect of turbulent water flow could be a decrease on the melt rates. However, these scenarios are outside the scope of this master thesis. It requires a lot of computing power and time, since turbulent simulations need a good resolution on a sub meter scale in order to resolve eddy formation. Furthermore, they require small timesteps since it is a fast changing system. Hence, a turbulent flow scenario, which is possible with the Navier-Stokes equation, would be a topic for future investigation.

Resuming to the non stationary idea of subglacial drainage systems, it implies that subglacial systems are in constant change. The difference in flow velocities underlines this fact. For example, a lake drainage event can occur in the range of hours and day whereas creep flow of the ice will take years to fill the resulting gap, which the elastic responds cannot fill. Here, the experiment *sub\_m2* illustrates that the melt dynamics change with increasing water flow velocity even when regulated by the inflow channel width. Hence if a lake drainage event happens over a longer time scale and over an region of increased heat flux new subglacial reservoir can form. In the models the inflow of water is continuous over time but drainage events might happen over shorter time scales (months or even days (Wingham et al., 2006)). Such a drainage event might not have strong effects on melt dynamics underneath ice masses since the advective transport would transport the heat away and the diffusive transport would not be fast enough in order to act on the melt rate behaviour.

Concluding for an ice sheet the results show that water filled cavities can form at the base. When an input water flow is assumed from either a reservoir like a subglacial lake, a supraglacial waters system or the base of an ice sheet as catchment area the size of the cavity will deform over time. Assuming the geothermal heat flux is known in that region and the shape of the cavity, which is easily achieved by the use of Ground Penetrating Radar, than implication of the water flow velocities can be made. Greater deformation of the cavity in direction of flow would result from higher water flow velocities. As until now

little is known about water flow velocities underneath ice masses, this could be a future approach in order to determine the flow velocities. Certain difficulties come along with that approach like bottom topography or state of evolution. Nevertheless it could be a first step into quantifying water flow velocities.

All experiments evolve a subglacial water layer with the help of an increase geothermal heat flux. Hence, subglacial water can only be formed in regions with increased geothermal heat flux. The study by Llubes et al. (2006) calculates enhanced melt rates in regions of increased heat flux, which applies for West Antarctica and the coastal areas. These are the preferred regions for the appearances of subglacial systems. Lakes can grow in regions, which are sinks in the hydrostatic potential. In lakes the water flow is rather slow in comparison to subglacial drainage systems. Even if water flows in the order of  $\text{mm s}^{-1}$  have an impact of the formation of a cavity. It will propagate downstream and change its shape over time. Hence, increased geothermal is an indicator for if subglacial water can be present but it will not determine the form of subglacial water flow.

This Master thesis only deals with 2D numerical models but still an implication on 3D

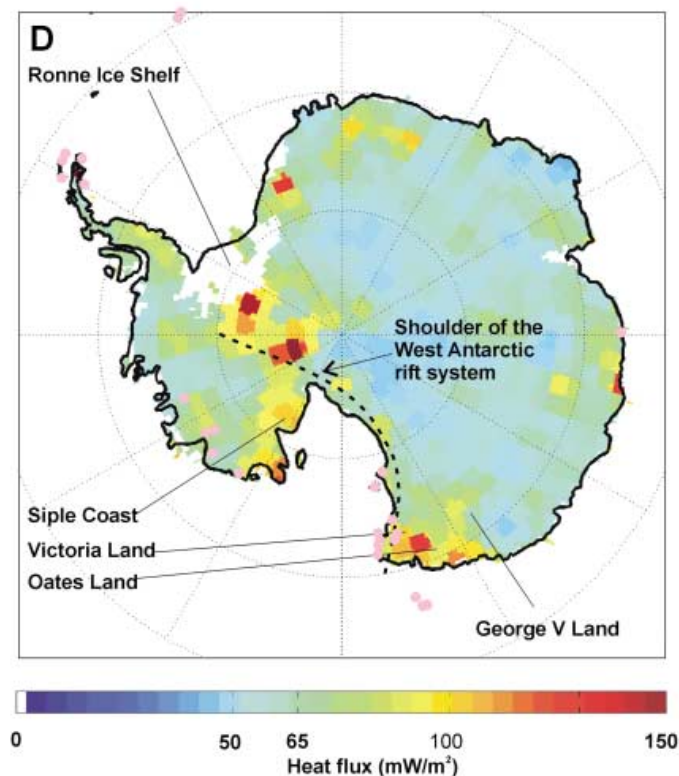


Figure 5.5.: Geothermal heat flux derived form satellite data (Maule et al., 2005)

scenario can be made in order to solve one part of the question: how can subglacial channels form themselves. For example, if the heat source is along a ridge (rift system see Fig. 5.5), it would create a cavity over this ridge. A stretched cavity could evolve over the ridge. If the ridge is orthogonal to the direction of ice flow a channel perpendicular to the ice

flow would evolve (see schematic illustration Fig. 5.7 B)). The experiments demonstrate that cavities will form over time due to the flow of water and the transportation of heat. Since, the experiments are in 2D but if they are interpolated in a third dimension a channel like feature would form. Further, experiment *sub\_m2-flat* shows that channels can form a simple sheet flow if the inflow velocity reaches a critical value. The experiments let conclude that a velocity above an order of  $10 \text{ cm}^{-1}$  are necessary to evolve a channelized water flow system in the direction of water flow.

On the other hand a cavity in the ice could be created (see Fig. 5.7 A)) at lower flow velocities in the region of increased geothermal heat flux. Until now cavities were assumed with a depression in bedrock topography (see Fig. 5.6). This Master thesis would suggest possible larger scaled cavities in areas with increased geothermal heat flux and low water flow velocities. Hence, a depression in the bedrock is not necessarily for the formation of a cavity.

As discussed above these subglacial systems are not in a steady state. The experiments show that the shape and position of the cavity is time dependent. The cavities will propagate in the downstream direction. An effect, which is not directly studied in this thesis, is the movement of the cavity with the ice flow. Ice velocities at the base are normally slow but can increase in region, where the water lubricates the ice. This would lead to a potential propagation of the cavity outside the regions of increased geothermal heat flux. In that case the cavity could refreeze and a cyclic behaviour could establish with a switch between melting, propagation and refreezing.

Concluding, the experiments illustrate that subglacial water underneath ice masses is in a highly dynamic system and melt dynamics are strongly influenced by variation in water flow velocities.

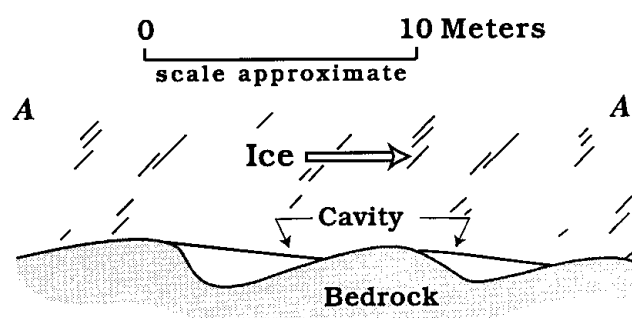


Figure 5.6.: Cavity in region where the bed topography show a depression from Fountain and Walder (1998)

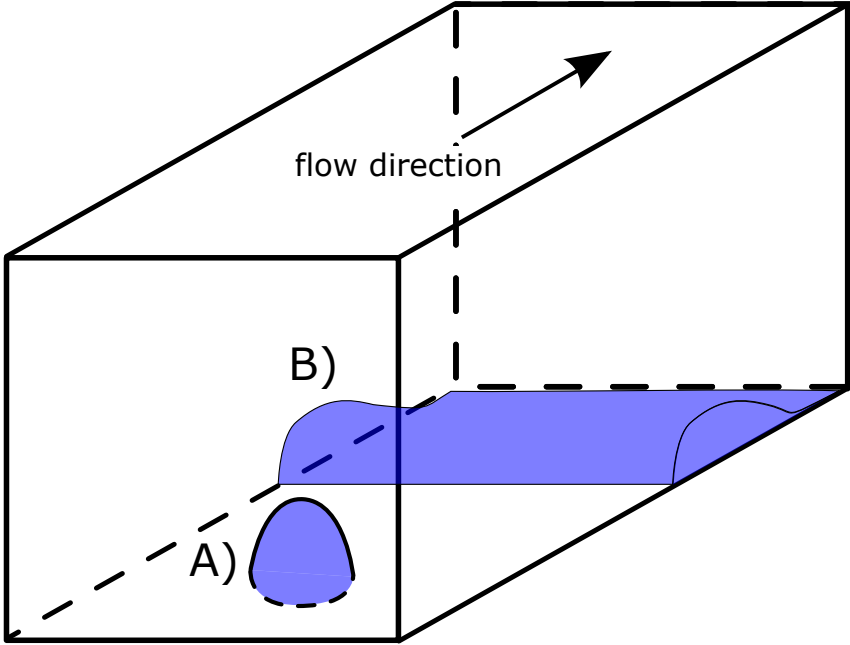


Figure 5.7.: Schematic illustration of Channel perpendicular to ice flow.



## 6. Conclusion and Outlook

In the last decade the importance of subglacial water rose in the field of glaciology. Water at the bedrock has effects on ice dynamics and melt regimes. For example, lake drainage events result in depressions at ice surface or the simple presence of water lubricates the ice masses. Up to now, little is known about subglacial systems underneath ice masses. In mountain glaciers a variety of investigations have been done like dye tracing and gauging stations measurements. Applying these methods to ice sheet is nearly impossible, due to logistic reasons. Hence, this master thesis attempts to model subglacial processes with the help of the Finite Element Method. The numerical model couples ice and water flow with the use of the Navier-Stokes equation to thermodynamic problem, which is a new approach in subglacial water modelling. In order to solve the heat fluxes the state of the art enthalpy description is used from Aschwanden et al. (2012). It enables the numerical model to calculate temperature and water content at once.

As still little is known about subglacial water flow velocities, three main sensitivity experiments study the effect of melt rate dynamics linked to different flow conditions in water and ice. The established 2D conceptual model represents a subset of an ice sheet, which is heated at the bottom by the geothermal heat flux. During the simulation a water layer develops and starts to flow. In different experiments four inflow velocities are tested. All experiments show that the simulated water velocities affect the melt rate. There is a critical flow velocity above the order of  $\text{cm s}^{-1}$ , which shows a switch in the melt rate behaviour. Further, the experiments prove a positive feedback between melt rate, cavity shape and water flow. If one of the components changes it will result in a change of the other two as well.

From these findings it can be reasoned that subglacial drainage systems are in constant changing systems, if water flows at velocities above the critical velocity. Lower inflow velocities indicate a more dome like water lens. Since water velocities underneath ice masses are unknown, the cavity shape could give a hint on which side of the spectrum they are orientated.

Future work would include the numerical model in 3D in order to investigate the evolution of the described perpendicular channel. Further, the still unsolved stability problems with the coupling of the ALE to the ice and water flow in order to build case studies e.g. the North Greenland Ice Stream (NEGIS) or mountain glaciers in order to compare model results to field data. Moreover, this could lead even to modelling of subglacial channels which are transported with the ice flow and show a potential closing by creep flow. Further,

future ice models could implement the water thickness into the gliding law. This would improve ice dynamics models, which play as well a key role in future climate change models.

These future experiments can be based on the results of this Master thesis. Here, it is shown that subglacial water and its movement has an enormous impact on melt dynamics. Hence, this Master thesis proves that coupling ice and water flow with the Navier-Stokes equation is possible and brings modelling of subglacial water a great step further than just its parametrisation.

# Acknowledgement

I want to thank specially these persons:

- Angelika Humbert, who supervised this Master thesis and has always a clever idea and an inspiration for new views.
- Thorsten Bickert, who taught me a lot about Stable Isotopes and the geology of the Alps and further he friendly agreed to be the second supervisor of this master thesis.
- Martin Rückamp, who I could ask anything about Comsol and he knew every trick there is to get Comsol to convergence.
- Prof. Dr.-Ing. Ralf Müller, Caroline Plate and Julia Christmann from the Technische Universität Kaiserslauten for their good discussion and cooperation.
- Further I thank the whole Glaciology group at AWI for their great company.



## Bibliography

- Arnold, N., Richards, K., Willis, I., and Sharp, M. (1998). Initial results from a distributed, physically based model of glacier hydrology Abstract. *Hydrological Processes*, 12(February 1997):191–219.
- Aschwanden, A., Bueler, E., Khroulev, C., and Blatter, H. (2012). An enthalpy formulation for glaciers and ice sheets. *Journal of Glaciology*, 58(209):441–457.
- Benn, D. I. and Evans, D. J. A. (2010). *Glaciers and glaciation*. Hodder Education, London, 2nd ed. edition.
- Beyer, S. (2014). Viscoelastic modelling of grounding line migration. Master's thesis, University of Hamburg.
- Codina, R. (1998). Comparison of some finite element methods for solving the diffusion-convection-reaction equation. *Computer Methods in Applied Mechanics and Engineering*, 156:185–210.
- COMSOL Inc (2014). *Comsol Multiphysics Reference Manual*. COMSOL MULTIPHYSICS Inc.
- COMSOL Inc (2015). COMSOL Multiphysics.
- Cuffey, K. M. and Paterson, W. (2010). *The physics of glaciers*. Elsevier [u.a.], Amsterdam [u.a.], 4. [rev.] edition.
- Delworth, T. L. (2008). Chapter 4. The Potential for Abrupt Change in the Atlantic Meridional Overturning Circulation. In *SAP 3.4: Abrupt Climate Change Voss*, pages 258–359. US Global Change Research Program USGCRP.
- Fountain, A. and Walder, J. (1998). Water flow through temperate glaciers. *Reviews of Geophysics*, 36(97):299–328.
- Fricker, H. A., Scambos, T., Bindschadler, R., and Padman, L. (2007). An active subglacial water system in West Antarctica mapped from space. *Science (New York, N.Y.)*, 315(5818):1544–8.
- Glasser, N. F. (2013). 8.6 Water in Glaciers and Ice Sheets. In Shroder, J. F., editor, *Treatise on Geomorphology*, pages 61–73. Academic Press, San Diego.

- Glen, J. W. (1955). The Creep of Polycrystalline Ice. *Proceedings of the Royal Society of London A: Mathematical, Physical and Engineering Sciences*, 228(1175):519–538.
- Greve, R. and Blatter, H. (2009). *Dynamics of ice sheets and glaciers*. Springer, Dordrecht; New York.
- Greve, R. and Hutter, K. (1995). Polythermal three-dimensional modelling of the Greenland ice sheet with varied geothermal heat flux. *Annals of Glaciology*, 21:8–12.
- Gulley, J., Benn, D., Screaton, E., and Martin, J. (2009). Mechanisms of englacial conduit formation and their implications for subglacial recharge. *Quaternary Science Reviews*, 28(19-20):1984–1999.
- Hauke, G. and Hughes, T. J. R. (1998). A comparative study of different sets of variables for solving compressible and incompressible flows. *Computer Methods in Applied Mechanics and Engineering*, 153:1–44.
- Helm, V., Humbert, A., and Miller, H. (2014). Elevation and elevation change of Greenland and Antarctica derived from CryoSat-2. *The Cryosphere*, 8(4):1539–1559.
- Hindmarsh, A. C., Brown, P. N., Grant, K. E., Lee, S. L., Serban, R., Shumaker, D. E., and Woodward, C. S. (2005). SUNDIALS: Suite of Nonlinear and Differential/Algebraic Equation Solvers. *ACM Trans. Math. Softw.*, 31(3):363–396.
- Kamb, B. (1987). Glacier surge mechanism based on linked cavity configuration of the basal water conduit system. *Journal of Geophysical Research*, 92(6):9083.
- Kleiner, T. and Humbert, A. (2014). Numerical simulations of major ice streams in western Dronning Maud Land, Antarctica, under wet and dry basal conditions. *Journal of Glaciology*, 60(219):1–18.
- Kleiner, T., Rückamp, M., Bondzio, J. H., and Humbert, A. (2015). Enthalpy benchmark experiments for numerical ice sheet models. *The Cryosphere*, 9(1):217–228.
- Kundu, P. K., Cohen, I. M., and Dowling, D. R. (2014). *Fluid Mechanics*. Elsevier, Boston, 5 edition.
- Lliboutry, L. A. (1987). *Very Slow Flows of Solids, Basics of Modeling in Geodynamics and Glaciology*, volume 25. Martinus Nijhoff Publishers.
- Llubes, M., Lanseau, C., and Rémy, F. (2006). Relations between basal condition, subglacial hydrological networks and geothermal flux in Antarctica. *Earth and Planetary Science Letters*, 241(3-4):655–662.
- Maule, C. F., Purucker, M. E., Olsen, N., and Mosegaard, K. (2005). Heat flux anomalies in Antarctica revealed by satellite magnetic data. *Science (New York, N.Y.)*, 309:464–467.

- Moran, M. J. and Shapiro, H. N. (2006). *Fundamentals of Engineering Thermodynamics*. Wiley.
- Murray, T. (2003). Is there a single surge mechanism? Contrasts in dynamics between glacier surges in Svalbard and other regions. *Journal of Geophysical Research*, 108(B5):2237.
- Nye, J. F. (1957). The Distribution of Stress and Velocity in Glaciers and Ice-Sheets. *Proceedings of the Royal Society of London A: Mathematical, Physical and Engineering Sciences*, 239(1216):113–133.
- Oreskes, N., Shrader-Frechette, K., and Belitz, K. (1994). Verification, Validation, and Confirmation of Numerical Models in the Earth Sciences. *Science*, 263(5147):641–646.
- Pattyn, F. (2010). Antarctic subglacial conditions inferred from a hybrid ice sheet/ice stream model. *Earth and Planetary Science Letters*, 295(3-4):451–461.
- Pattyn, F., Perichon, L., Aschwanden, A., Breuer, B., de Smedt, B., Gagliardini, O., Gudmundsson, G. H., Hindmarsh, R. C. A., Hubbard, A., Johnson, J. V., Kleiner, T., Konovalov, Y., Martin, C., Payne, A. J., Pollard, D., Price, S., Rückamp, M., Saito, F., Souček, O., Sugiyama, S., and Zwinger, T. (2008). Benchmark experiments for higher-order and full-Stokes ice sheet models (ISMIP HOM). *The Cryosphere*, 2(2):95–108.
- Rahmstorf, S. (2006). Thermohaline Ocean Circulation. In *Encyclopedia of Quaternary Sciences*, pages 1–10. Elsevier, Amsterdam.
- Rignot, E., Mouginot, J., and Scheuchl, B. (2011). Ice Flow of the Antarctic Ice Sheet. *Science*, 333(6048):1427–1430.
- Schlichting, H. and Gersten, K. (1997). *Grenzschicht-Theorie*. Springer, Berlin.
- Shepherd, A., Ivins, E. R., Geruo, A., Barletta, V. R., Bentley, M. J., Bettadpur, S., Briggs, K. H., Bromwich, D. H., Forsberg, R., Galin, N., and Others (2012). A reconciled estimate of ice-sheet mass balance. *Science*, 338(6111):1183–1189.
- Siegert, M. J. (2000). Antarctic subglacial lakes. *Earth-Science Reviews*, 50(1-2):29–50.
- Sigloch, H. (2008). *Technische Fluidmechanik*. Springer Berlin Heidelberg / New York, 6. edition edition.
- Solomon, S., Qin, D., Manning, M., Maquis, M., Averyt, K., Tignor, M. M., Miller, H. L., and Chen, Z. (2007). *Climate Change 2007, the physical science basis. Contribution of Working Group 1 to the Fourth Assessment Report of the Intergovernmental Panel on Climate Change*. Cambridge University Press.

Stefan, J. (1888). Ueber einige Probleme der Theorie der Waermeleitung. *Wien. Ber.*, 98:473–484.

Wingham, D. J., Siegert, M. J., Shepherd, A., and Muir, A. S. (2006). Rapid discharge connects Antarctic subglacial lakes. *Nature*, 440(April):1033–1036.

## List of Figures

1.1.	Schematic drawing of mass transported in ice sheets and velocity fields. .	2
1.2.	Surfaces velocities of Antarctica (Rignot et al., 2011) . . . . .	3
1.3.	Schematic drawings of subglacial drainage systems (modified after Benn and Evans (2010)) . . . . .	4
2.1.	Figure of a sheared block of ice and the resulting shear angle . . . . .	11
2.2.	Schematic drawing of geometry setup . . . . .	12
3.1.	Screenshot of Comsol Multiphysics <sup>®</sup> GUI . . . . .	18
3.2.	Smoothed Heaviside function by the Comsol build in function <code>f1c2hs</code> of the liquid parameter smoothed over $10^{-5}$ m . . . . .	19
3.3.	Top branch of the <i>Heat transfer node</i> . . . . .	21
3.4.	Schematic solver diagram . . . . .	30
4.1.	Distribution of the geothermal heat flux applied on the boundary water/lithosphere . . . . .	32
4.2.	Shape of the preset cavity with a 2 m size. . . . .	33
4.3.	Verification of basal melt . . . . .	35
4.4.	Zoom of temperature graph during the warming phase in order to visualize the increasing temperature. . . . .	36
4.5.	Schematic drawing of ISMIP-HOM experiment D . . . . .	36
4.6.	Verification of <i>sub_m0-p</i> . . . . .	37
4.7.	Exp. <i>sub_m1</i> : Melt rates and normalized water velocities . . . . .	38
4.8.	Exp. <i>sub_m1</i> : Water thickness . . . . .	39
4.9.	Exp. <i>sub_m1</i> : Cavity deformation . . . . .	40
4.10.	Exp. <i>sub_m2</i> : Melt rates and normalized water velocities . . . . .	41
4.11.	Exp. <i>sub_m2</i> : Water thickness . . . . .	42
4.12.	Exp. <i>sub_m2</i> : Cavity deformation . . . . .	42
4.13.	Exp. <i>sub_m2-flat</i> : Cavity deformation . . . . .	43
4.14.	Exp. <i>sub_m2-flat</i> : Melt rates and water velocities . . . . .	44
4.15.	Exp. <i>sub_m3</i> : Melt rates . . . . .	45
4.16.	Exp. <i>sub_m3</i> : Water velocities . . . . .	45
4.17.	Exp. <i>sub_m3</i> : Temperature field . . . . .	46
4.18.	Exp. <i>sub_m3</i> : melt rates for the two ice velocities . . . . .	46

---

5.1. Pressure melting point temperature $T_{pmp}$ dependent on the depth in an ice sheet with constant density ( $\rho_{ice} = 910 \text{ kg m}^{-3}$ ) . . . . .	47
5.2. Convergence graph of experiment <i>sub_m2</i> . . . . .	49
5.3. Schematic illustration of positive feedback . . . . .	52
5.4. Schematic cavity transformation at critical velocities. . . . .	54
5.5. Geothermal heat flux derived from satellite data (Maule et al., 2005) . .	59
5.6. Cavity in region where the bed topography show a depression from Fountain and Walder (1998) . . . . .	60
5.7. Schematic illustration of Channel perpendicular to ice flow. . . . .	61

## List of Tables

3.1. Default physical global parameters . . . . .	18
3.2. Default geometry parameters and variables . . . . .	19
3.3. Heat transfer parameters and variables . . . . .	22
3.4. Laminar flow 1 + 2 variables and parameters . . . . .	26
3.5. Solver: table of termination values . . . . .	29
4.1. List of all experiments . . . . .	32
4.2. Exp. <i>sub_m1</i> : Overview of key quantities of exp. <i>sub_m1</i> . . . . .	39
4.3. Exp. <i>sub_m2</i> : Overview of key quantities of exp. <i>sub_m2</i> . . . . .	41
4.4. Melt rate values of exp. <i>sub_m3</i> . . . . .	44
A.1. Abbreviations register . . . . .	75



## A. Appendix

In the included CD you will find this Master thesis in Pdf format.

### Abbreviations

Table A.1.: Abbreviations register

Abbreviation	Value	[Unit]	Description
$g$	9.81	$[m s^{-1}]$	: Gravity acceleration
$\rho_i$	910	$[kg m^{-3}]$	: Density of ice
$\rho_w$	1000	$[kg m^{-3}]$	: Density of water
$\mathbf{v}$		$[m s^{-1}]$	: Velocity vector
$\alpha$		$[\circ]$	: Angle of slope inclination
$\boldsymbol{\sigma}$		$[Pa]$	: Stress tensor
$\boldsymbol{\sigma}^D$		$[Pa]$	: Diviatoric part of stress tensor
$t$		$[s]$	: Time
$p$		$[Pa]$	: Pressure
$\mathbf{I}$			: Identity matrix
$\mathbf{f}$			: Volume forces
$\eta_i$	$\approx 10^{14}$	$[Pa \cdot s]$	: Viscosity of ice
$\eta_w$	$1.78 \cdot 10^{-3}$	$[Pa \cdot s]$	: Viscosity of water
$C_i$	2009	$[J kg^{-1} K^{-1}]$	: Heat capacity of ice
$C_w$	4216.278	$[J kg^{-1} K^{-1}]$	: Heat capacity of water
$E_j$		$[J kg^{-1} K^{-1}]$	: Enthalpy of ice ( $j = i$ ) and water ( $j = w$ )
$T$		$[K]$	: Temperature
$\omega$		$[\%]$	: Water content
$\mathbf{q}_j$		$[W m^{-2}]$	: Heat flux of ice ( $j = i$ ) and water ( $j = w$ )
$a_b$		$[mm a^{-1}]$	: Melt rate
$\dot{\epsilon}$		$s^{-1}$	: strain rate
$\dot{\epsilon}_e$		$s^{-1}$	: effective strain rate
$E$			: Enhancement factor
$A$		$[Pa^{-3} s^{-1}]$	: Rate factor
$h$		$[m]$	: Size of mesh element
$C$	0.5		: Courant-Friedrich-Levi Condi- tion number
$spy$	31556926	$[s a^{-1}]$	Seconds per year
$\beta$	$7.910^{-8}$	$[K Pa^{-1}]$	Clausius-Clapyron constant
$beta2$	$50 \dots \infty$	$[Pa a m^{-1}]$	Friction coefficient